Draft version August 17, 2011
Preprint typeset using LaTeX style emulateapj v. 5/25/10

arXiv:1108.3081v1 [astro-ph.CO] 15 Aug 2011

STRUCTURE FORMATION IN THE SYMMETRON MODEL

Anne-Christine Davis[2, δ], Baojiu Li[2,3, λ], David F. Mota[1, μ], and Hans A. Winther[1, ω]
[1]Institute of Theoretical Astrophysics, University of Oslo, 0315 Oslo, Norway
[2]DAMTP, Centre for Mathematical Sciences, University of Cambridge, Wilberforce Road, Cambridge CB3 0WA, UK and
[3]Kavli Institute for Cosmology Cambridge, Madingley Road, Cambridge CB3 0HA, UK

Draft version August 17, 2011

ABSTRACT

Scalar fields, strongly coupled to matter, can be present in nature and still be invisible to local experiments if they are subject to a screening mechanism. The symmetron is one such mechanism which relies on restoration of a spontaneously broken symmetry in regions of high density to shield the scalar fifth force. We have investigated structure formation in the symmetron model by using N-body simulations and find strong observable signatures in both the linear and nonlinear matter power spectrum and on the halo mass function. The mechanism for suppressing the scalar fifth force in high density regions is also found to work very well.

1. INTRODUCTION

Our current standard model of cosmology, ΛCDM, has been very successful in explaining a large range of observations probing a vast range in length scales. We should nevertheless be open for the possibility that ΛCDM is just a first order approximation of some more fundamental theory. Many theories of high energy physics, like string theory and supergravity, predict light gravitationally coupled scalar fields (see e.g. Binetruy (2006); Linde (2008) and references therein). These scalars may play the role of dark energy (quintessence). If these scalar fields have non-minimal coupling to matter fields, then they could mediate extra forces which are potentially detectable in local experiments.

Over the last decades, several laboratory and solar system experiments have tried to detect a sign of such fundamental coupled scalar fields (Adelberger 2002; Hoskins et al. 1985; Decca et al. 2007; Bertotti et al. 2003), but the results so far show no signature of them. Naively, the results of these experiments have ruled out any such scalar fields. However, one should bear in mind that a coupled scalar field might exist but is undetected just because it is either very weakly coupled or very heavy.

To this day we know three types of theoretical mechanisms (see Khoury (2010) for a review) that can explain why such light scalars, if they exist, may not be visible to experiments performed near the Earth. One such class, the chameleon mechanism (Khoury & Weltman 2004; Brax et al. 2004; Clifton et al. 2005; Mota & Barrow 2004a,b), operates when the scalars are coupled to matter in such a way that their effective mass depends on the local matter density. In space, where the local mass density is low, the scalars would be light and deviations from General Relativity would be observed. But near the Earth, where experiments are performed, the local mass density is high and the scalar field would acquire a heavy mass making the interactions short range and therefore unobservable.

ω Email address: h.a.winther@astro.uio.no
μ Email address: d.f.mota@astro.uio.no
λ Email address: b.li@damtp.cam.ac.uk
δ Email address: a.c.davis@damtp.cam.ac.uk

The second mechanism, the Vainshtein mechanism (Vainshtein 1972; Deffayet et al. 2002; Arkani-Hamed et al. 2003), operates when the scalar has derivative self-couplings which become important near matter sources such as the Earth. The strong coupling near sources essentially cranks up the kinetic terms, which translates into a weakened matter coupling. Thus the scalar screens itself and becomes invisible to experiments. This mechanism is central to the phenomenological viability of braneworld modifications of gravity and galileon scalar theories (Dvali et al. 2000; de Rham et al. 2008; Nicolis et al. 2008; Hinterbichler et al. 2010; Mota et al. 2010; Gabadadze 2009; de Rham 2010; Brax et al. 2011a).

The last mechanism, the one explored in this paper, is the symmetron mechanism (Hinterbichler & Khoury 2010; Hinterbichler et al. 2011; Olive & Pospelov 2008; Brax et al. 2011b). In this mechanism, the vacuum expectation value (VEV) of the scalar depends on the local mass density, becoming large in regions of low mass density, and small in regions of high mass density. By taking the coupling of the scalar to matter to be proportional to the VEV, we can have a viable theory where the scalar couples with gravitational strength in regions of low density, but is decoupled and screened in regions of high density. This is achieved through the interplay of a symmetry breaking potential and a universal quadratic coupling to matter.

In vacuum, the scalar acquires a VEV which spontaneously breaks the $\mathbb{Z}_2$ symmetry $\phi \to -\phi$. In the regions of sufficiently high matter density, the field is confined near $\phi = 0$, and the symmetry is restored. The fifth force arising from the matter coupling is proportional to ϕ making the effects of the scalar small in high density regions.

As opposed to Chameleons, where the strongest constraints (Mota & Shaw 2007; Brax et al. 2010b, 2008; Gannouji et al. 2010; Gies et al. 2008; Brax et al. 2007a,b; Mota & Shaw 2006) comes from laboratory experiments which in effect washes out any observable effects in the solar system, the symmetron predicts a host of observational signatures in experiments designed to look for deviations from GR, which are just below the currents bounds and within reach of the next generation experi-

ments.

The cosmology of coupled scalar field models are usually strongly constrained by local gravity experiments, which could put limits on the range and the coupling strength of the scalar field. There do exist several cases in which signatures on the linear perturbations are found, but in most cases the range of the field is well below linear scales. To proceed into the region of nonlinear structure formation one can use the spherical collapse model to obtain the qualitative behavior, but in order to obtain accurate quantitative results deep into the nonlinear regime one is almost required to perform N-body simulations.

Studies of coupled scalar field models by using N-body simulations (Zhao et al. 2011a; Brax et al. 2011c; Li & Barrow 2011a,b; Li et al. 2011a; Zhao et al. 2010; Li & Zhao 2010; Baldi et al. 2010; Baldi 2009) have revealed several interesting signatures which can in principle be detected by observations in the near future. For example, in Zhao et al. (2011b) it was found that $f(R)$ theories can give rise to a dependence on the environment of the dynamical to lensing mass ratio of halos; an observable feature that is not found in ΛCDM.

In this article we will study the effects a symmetron field has on structure formation. By performing high resolution N-body simulations we demonstrate explicitly how the Symmetron mechanism works in screening the fifth force and obtain observables as the matter power spectrum and the mass function.

2. THE SYMMETRON MODEL

The action governing the dynamics of the symmetron model is given by

$$S = \int dx^4\sqrt{-g}\left[\frac{R}{2}M_{\rm pl}^2 - \frac{1}{2}(\partial\phi)^2 - V(\phi)\right] + S_m(\tilde{g}_{\mu\nu},\psi_i) \quad (1)$$

where g is the determinant of the metric $g_{\mu\nu}$, R is the Ricci scalar, ψ_i are the different matter fields and $M_{\rm pl} \equiv \frac{1}{\sqrt{8\pi G}}$ where G is the bare gravitational constant. The matter fields couple to the Jordan frame metric $\tilde{g}_{\mu\nu}$ via a conformal rescaling of the Einstein frame metric $g_{\mu\nu}$ given by

$$\tilde{g}_{\mu\nu} = A^2(\phi)g_{\mu\nu} \quad (2)$$

The coupling function $A(\phi)$ is chosen to be an even polynomial in ϕ (to be compatible with the $\phi \to -\phi$ symmetry)

$$A(\phi) = 1 + \frac{1}{2}\left(\frac{\phi}{M}\right)^2 + \mathcal{O}\left(\frac{\phi^4}{M^4}\right) \quad (3)$$

described by a single mass scale M. For the range of parameters we are interested in we have $\left(\frac{\phi}{M}\right)^2 \ll 1$, thus, we can neglect the higher order correction terms. The potential is chosen to be of the symmetry breaking form

$$V(\phi) = V_0 - \frac{1}{2}\mu^2\phi^2 + \frac{1}{4}\lambda\phi^4 \quad (4)$$

where V_0 is a cosmological constant (CC). We will for simplicity absorb all contributions to the CC into V_0 by simply putting $V_0 \equiv \Lambda$. We will later see that Λ must be taken to be the usual CC to obtain late time acceleration of the Universe. The field equation for ϕ follows from the variation of the action Eq. (1) with respect to ϕ and reads

$$\Box\phi = V_{{\rm eff},\phi} \quad (5)$$

The effective potential is given in terms of the trace, T_m, of the matter energy-momentum tensor by

$$V_{\rm eff}(\phi) = \frac{1}{2}\left(-\frac{T_m}{M^2} - \mu^2\right)\phi^2 + \frac{1}{4}\lambda\phi^4 \quad (6)$$

$$= \frac{1}{2}\left(\frac{\rho_m}{M^2} - \mu^2\right)\phi^2 + \frac{1}{4}\lambda\phi^4 \quad (7)$$

depending on the two mass scales μ, M and the dimensionless coupling constant λ. It is convenient to define the critical matter density (and the critical redshift)

$$\rho_{\rm SSB} \equiv \mu^2 M^2 = 3H_0^2 M_{\rm pl}^2 \Omega_m (1+z_{\rm SSB})^3 \quad (8)$$

where Ω_m is the matter density parameter in the Universe today and H_0 is the Hubble parameter. In regions where $\rho_m > \rho_{\rm SSB}$ (where ρ_m is the local matter density) the symmetry $\phi \to -\phi$ is upheld and the effective potential has a minimum at $\phi_{\rm min} = 0$, whereas in regions where $\rho_m < \rho_{\rm SSB}$ the symmetry is spontaneously broken and the field acquires a VEV

$$\phi_{\rm min} = \pm\phi_0\sqrt{1 - \frac{\rho_m}{\rho_{\rm SSB}}} \quad (9)$$

where $\phi_0 \equiv \frac{\mu}{\sqrt{\lambda}}$ is the symmetry breaking VEV for $\rho_m \to 0$. The mass of small fluctuations around the minimum of the effective potential is given by

$$m_\phi^2 \equiv V_{{\rm eff},\phi\phi} = \left(\frac{\rho_m}{\rho_{\rm SSB}} - 1\right)\mu^2 + 3\lambda\phi_{\rm min}^2 = \begin{cases} \mu^2\left(\frac{\rho_m}{\rho_{\rm SSB}} - 1\right), & \rho_m > \rho_{\rm SSB} \\ 2\mu^2\left(1 - \frac{\rho_m}{\rho_{\rm SSB}}\right), & \rho_m < \rho_{\rm SSB} \end{cases} \quad (10)$$

The symmetron field acquires the longest range, $\lambda_\phi \equiv \frac{1}{m_\phi}$, in low density regions where

$$\lambda_\phi = \lambda_0 \equiv \frac{1}{\sqrt{2}\mu} \quad (11)$$

For future convenience we introduce the dimensionless quantity $L \equiv \frac{\lambda_0}{{\rm Mpc}/h}$, which is the maximum range of the symmetron mediated force in units of ${\rm Mpc}/h$.

The gravitational field equation for $g_{\mu\nu}$ is given by

$$G_{\mu\nu} = 8\pi G T_{\mu\nu} \quad (12)$$

where the total energy-momentum tensor $T_{\mu\nu}$ is the sum of the matter and scalar field parts:

$$T_{\mu\nu} = A(\phi)T_{\mu\nu}^m + \phi_{;\mu}\phi_{;\nu} - g_{\mu\nu}\left(\frac{1}{2}(\partial\phi)^2 + V(\phi)\right) \quad (13)$$

Note that the matter part itself is not conserved, but instead satisfies

$$\nabla_\nu T_m^{\mu\nu} = \frac{d\log A(\phi)}{d\phi}\left(T_m\nabla^\mu\phi - T_m^{\mu\nu}\nabla_\nu\phi\right) \quad (14)$$

In N-body simulations we are interested in describing the matter sector by particles and the energy-momentum tensor of an individual particle with mass m_0 at position $\mathbf{r_0}$ is given by

$$T_m^{\mu\nu}(\mathbf{r}) = \frac{m_0}{\sqrt{-g}}\delta(\mathbf{r}-\mathbf{r}_0)\dot{r}_0^\mu \dot{r}_0^\nu \tag{15}$$

where $\mathbf{r}$ is the general spatial coordinate. Taking the divergence of Eq. (12) and using the Bianchi identity we get the geodesic equation for the matter particles

$$\ddot{r}_0^\mu + \Gamma^\mu_{\alpha\gamma} r_0^\alpha r_0^\gamma = -\frac{d\log A(\phi)}{d\phi}\left(\nabla^\mu\phi + \dot{\phi}\dot{r}_0^\mu\right) \tag{16}$$

which for $A \equiv 1$ reduces to the standard geodesic equation in general relativity.

2.1. *The Symmetron Mechanism: Local Constraints*

From Eq. (16) we see that the symmetron field gives rise to a fifth force on the matter fields which, in the nonrelativistic limit, is given by

$$\vec{F}_\phi = \frac{\phi}{M^2}\vec{\nabla}\phi = \frac{\beta}{M_{\rm pl}}\left(\frac{\phi}{\phi_0}\right)\vec{\nabla}\phi \tag{17}$$

where we have introduced the coupling constant $\beta \equiv \frac{\phi_0 M_{\rm pl}}{M^2}$.

The static spherical symmetric solutions of the field equations were found in Hinterbichler & Khoury (2010). For two test masses in a region where $\phi = \phi_B$ it was shown that that the fifth force is simply

$$\frac{F_\phi}{F_N} = 2\beta^2\left(\frac{\phi_B}{\phi_0}\right)^2 \tag{18}$$

In a low density region ($\rho \ll \rho_{\rm SSB}$) we have $\phi_B = \phi_0$ and the fifth force is comparable with gravity for $\beta = \mathcal{O}(1)$.

For very large bodies, the situation is quite different. The symmetry is restored in the interior of the body and the fifth force on a test mass outside becomes

$$\frac{F_\phi}{F_N} = 2\beta^2\left(\frac{\phi_B}{\phi_0}\right)^2\frac{1}{\alpha}, \quad \alpha^{-1} = 2\frac{\rho_{\rm SSB}}{\rho_{\rm body}}\left(\frac{\lambda_0}{R_{\rm body}}\right)^2 \tag{19}$$

The fifth force is suppressed by a factor $\alpha^{-1} \ll 1$ – similar to the thin shell factor found in chameleon theories (Khoury & Weltman 2004).

We also see that if the test masses are inside a screened region $\left(\frac{\phi_B}{\phi_0} \ll 1\right)$ the force will be further suppressed.

Since the field is long ranged (and universally coupled) in almost all situations today the theory is best constrained by solar system experiments which have been performed with high precision.

It turns out that as long as our Galaxy is sufficiently screened ($10 \lesssim \alpha_G$), our Sun will also be screened and the combined effects discussed above are enough to evade the current parameterized post Newtonian (PPN) constraints.

By assuming that $\phi \to \phi_0$ outside our Galaxy, i.e. that our galactic neighborhood is not screened, these constraints were derived in Hinterbichler & Khoury (2010); Brax et al. (2011b), and require

$$M \lesssim 10^{-3} M_{\rm pl} \tag{20}$$

If the assumption about the value of ϕ outside our Galaxy, which is very likely to be true, can be relaxed then the bound above can be relaxed somewhat as well. The constraint on M turns into a constraint on the range of the field and the redshift in which the SSB takes place:

$$\lambda_0 \lesssim 2.3\sqrt{\frac{0.3}{\Omega_m}}(1+z_{\rm SSB})^{-3/2}{\rm Mpc}/h \tag{21}$$

Thus for transitions that take place close to the present, the fifth force can have a range of at most a few Mpc/h.

2.2. *Physical Parameters*

In the rest of this article, instead of working with the parameters $\{\mu, M, \lambda\}$, we will instead choose to work with the more physically intuitive quantities $\{L, \beta, z_{\rm SSB}\}$: the cosmological range of the fifth force in Mpc/h, the strength of the fifth force relative to gravity and the redshift at which the SSB takes place in the cosmological background.

The transformation between the two sets of parameters is given by

$$\frac{\mu}{H_0} = \frac{2998}{\sqrt{2}L} \tag{22}$$

$$\frac{M}{M_{\rm pl}} = 10^{-3}\sqrt{\frac{\Omega_m}{0.27}}\left(\frac{L}{2.36}\right)(1+z_{\rm SSB})^{3/2} \tag{23}$$

$$\lambda = \left(\frac{10^{60}H_0}{M_{\rm pl}}\cdot\frac{0.27}{\Omega_m}\right)^2\frac{1.38\cdot10^{-100}}{\beta^2 L^6(1+z_{\rm SSB})^6} \tag{24}$$

For typical parameters $L \sim \beta \sim 1$ and $z_{\rm SSB} \sim 0$ we have $\mu \sim 10^{-57}M_{\rm pl}$, $M \sim 10^{-3}M_{\rm pl}$ and $\lambda \sim 10^{-100}$: thus the symmetron is very weakly coupled.

We will choose to work with values of the parameters, that are close to the local constraints, and in which the symmetron can produce observable cosmological effects. This means we will be most interested in the parameter space $L = \mathcal{O}(1)$, $\beta = \mathcal{O}(1)$ and $0 \lesssim z_{\rm SSB} \lesssim 2$.

3. SYMMETRON COSMOLOGY

In this section we discuss the cosmological evolution of the symmetron field from the background evolution to linear perturbations and derive the nonrelativistic limits of the field equations to be implemented in the N-body code. The analysis in this section is mainly for comparison with the N-body simulations. For a more thorough discussion regarding the background cosmology and linear perturbations in the symmetron see Hinterbichler et al. (2011) and Brax et al. (2011b) respectively.

3.1. *Background Cosmology*

The background evolution of the symmetron in a flat Friedmann-Lemaitre-Robertson-Walker (FRLW) metric

$$ds^2 = -dt^2 + a^2(t)(dx^2+dy^2+dz^2) \tag{25}$$

is determined by the field equation

$$\ddot{\phi} + 3H\dot{\phi} + V_{{\rm eff},\phi} = 0 \tag{26}$$

together with the Friedman equations

$$3H^2M_{\rm pl}^2 = \rho_m A(\phi) + \rho_\phi \tag{27}$$

$$\dot{\rho}_m + 3H\rho_m = 0 \tag{28}$$

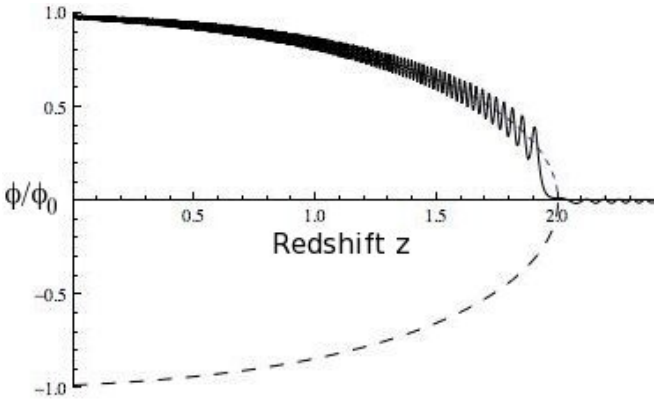

FIG. 1.— The background evolution of the symmetron for $\beta = 1$, $L = 1$ and $z_{\rm SSB} = 2$ together with the analytical background (dashed lines). The symmetry is broken at $z = 2$ and the field settles at one of the two branches.

where

$$\rho_\phi = \Lambda - \frac{1}{2}\mu^2\phi^2 + \lambda\phi^4 + \frac{1}{2}\dot{\phi}^2 \tag{29}$$

When the field follows the minimum of the effective potential we have

$$\left|\frac{\rho_\phi - \Lambda}{\Lambda}\right| \lesssim \frac{\mu^4}{\lambda\Lambda} = \beta^2\frac{\rho_{\rm SSB}}{\Lambda}\left(\frac{M}{M_{\rm pl}}\right)^2 \tag{30}$$

$$\lesssim 10^{-6}\beta^2(1+z_{\rm SSB})^3 \tag{31}$$

thus for $\beta, z_{\rm SSB} \sim \mathcal{O}(1)$ the dynamical part of the potential is too small to contribute significantly to the energy density of the Universe and we are left with the cosmological constant to account for dark energy.

In the same regime, the coupling function $A(\phi)$ satisfies

$$|A(\phi) - 1| = \frac{1}{2}\left(\frac{\phi}{M}\right)^2 \lesssim \beta^2\left(\frac{M}{M_{\rm pl}}\right)^2 \lesssim 10^{-6}\beta^2 \tag{32}$$

which is also too small to produce an observable effect on the background expansion. This implies that the symmetron evades Big Bang Nucleosyntesis (BBN) bounds on the variation of masses of the standard model particles (see Sec. (3.5.1)). It might be possible to make the symmetron responsible for dark energy by changing the form of the potential and coupling. One such modification was proposed in Hinterbichler et al. (2011), however it was shown that tuning of the parameters was required to yield the desired late time cosmology.

In Fig. (1) we see the background evolution $\phi(z)$ for $z_{\rm SSB} = 2$ together with the analytical minimum. Notice that the field does not immediately start to follow the minimum right after SSB. This has important consequences for the evolution of the perturbations which will be discussed in section 3.4.

3.2. *Linear perturbations*

The most general metric in a perturbed FLRW spacetime is given by

$$ds^2 = -(1+2\alpha)dt^2 - 2aB_{,i}dtdx^i \tag{33}$$
$$+a^2\left((1+2\psi)\delta_{ij} + 2\gamma_{,i;j}\right)dx^i dx^j$$

where the covariant derivative is given in terms of the spatial metric, which in the case of our flat background reduces to δ_{ij}. We decompose the field ϕ into the background and perturbated parts: $\phi(\mathbf{x},t) = \overline{\phi}(t) + \delta\phi(\mathbf{x},t)$. The energy-momenntum tensor of nonrelativistic matter can be decomposed as

$$T^0_0 = -\rho_m(1+\delta_m), \quad T^0_i = -\rho_m v_{,i} \tag{34}$$

where v is the peculiar velocity of nonrelativistic matter and δ_m is the matter density perturbation defined by

$$\delta_m \equiv \frac{\delta\rho_m}{\rho_m} - \frac{\dot{\rho}_m}{\rho_m}v \equiv \frac{\delta\rho_m}{\rho_m} \quad \text{in the comoving gauge} \tag{35}$$

The equation determining the evolution of the perturbations, neglecting anisotropic stresses, follows from the Einstein equations. The scalar perturbations can be read off from the formulation of (Hwang & Noh 2002), which is independent of gauge. In the following we use units of $M_{\rm pl} \equiv 1$. After solving for the different metric potentials we find that the scalar perturbations, in the comoving gauge ($v = 0$) are determined by

$$\ddot{\delta}_m + 2H\dot{\delta}_m - \frac{1}{2}\rho_m\delta_m \tag{36}$$
$$-\frac{\phi\delta\phi}{M^2}\left(6H^2 + 6\dot{H} + \Omega_m H^2 - \frac{k^2}{a^2} + 2\dot{\phi}^2\right)$$
$$-\frac{\phi}{M^2}\left(\ddot{\delta\phi} + 5H\dot{\delta\phi}\right) - \frac{2\dot{\phi}}{M^2}\left(\dot{\delta\phi} + H\delta\phi\right)$$
$$+V_{{\rm eff},\phi}\left(1 + \frac{1}{M^2}\right)\delta\phi - 2\dot{\phi}\dot{\delta\phi} = 0$$

$$\ddot{\delta\phi} + \left(3H + \frac{2\phi\dot{\phi}}{M^2}\right)\dot{\delta\phi} + \frac{\phi\rho_m\delta_m}{M^2} - \dot{\phi}\dot{\delta}_m \tag{37}$$
$$+\left(m_\phi^2 + \frac{k^2}{a^2} - \frac{2\phi}{M^2}V_{{\rm eff},\phi} + \frac{2\dot{\phi}^2}{M^2}\right)\delta\phi = 0$$

In studying the perturbations it is convenient to introduce the growth index

$$\gamma(z,k) = \frac{\log\left(\frac{d\log\delta_m}{d\log a}\right)}{\log(\Omega_m(z))}. \tag{38}$$

In ΛCDM we have $\gamma \approx 0.55$ (for $0.2 \lesssim \Omega_m \lesssim 0.3$), which is scale and almost redshift independent. In modified theories however, γ can have significant scale and redshift dependence as shown in Gannouji et al. (2010); Tsujikawa et al. (2009); Brax et al. (2008, 2010a); Mota & Winther (2011) for the case of chameleon/$f(R)$ models.

If we assume that the field is rolling slowly along the minimum we can neglect all terms proportional to $\dot{\phi}$ and the oscillating term $V_{{\rm eff},\phi}$. The perturbations in ϕ will evolve more slowly than the perturbations in δ_m for scales deep inside the Hubble radius, thus, the term $\rho_m\beta_{,\phi}\,\delta_m$ and $(m_\phi^2 + \frac{k^2}{a^2})\delta\phi$ will dominate over the $\delta\phi$ time derivatives in Eq. (37). Under these assumptions,

we can simplify Eq. (36) to

$$\ddot{\delta_m} + 2H\dot{\delta_m} = \frac{3}{2}\Omega_m H^2 \frac{G_{\rm eff}}{G}\delta_m \tag{39}$$

$$\frac{G_{\rm eff}}{G} = 1 + \frac{2\beta^2\phi^2/\phi_0^2}{1+\frac{a^2}{\lambda_\phi^2 k^2}} \tag{40}$$

which are the equations we use to integrate the perturbations.

At the time before SSB we have $\phi \approx 0$ and therefore $\frac{G_{\rm eff}}{G} = 1$. After SSB the field approaches the minimum $\phi_0 = \pm\frac{\mu}{\sqrt{\lambda}}$, in this regime we have

$$\frac{G_{\rm eff}}{G} = \begin{cases} 1 & \frac{a}{k} \gg \lambda_\phi \\ 1+2\beta^2 & \frac{a}{k} \ll \lambda_\phi \end{cases} \tag{41}$$

Thus small scales will feel a stronger gravitational constant.

In Fig. (2) we show the redshift evolution of γ for several different wavenumbers and in Fig. (3) we show contour plots for $\gamma(z=0)$ for two comoving wavenumbers.

The growth rate on really large scales ($k \lesssim 0.01h$/Mpc) is not affected by the symmetron fifth force unless $L, \beta \gg 1$. However on the smallest, linear scales we can still have a deviation from the predications of GR. Note that we have integrated the perturbations using the approximation Eq. (39) instead of the full equations Eq. (36-37). The explanation for this is given in Sec. (3.4).

3.3. *Linear power spectrum and the CMB*

In Fig. (4) we show the factional difference of the linear power spectrum of the symmetron to that of ΛCDM, defined as $\frac{\Delta P(k)}{P(k)} \equiv \frac{P(k)-P_{\Lambda CDM}(k)}{P_{\Lambda CDM}(k)}$. Notice that on linear scales ($k \lesssim 0.1h$/Mpc) the power spectrum is very close to ΛCDM. Going down to scales comparable to the length scale of the symmetron ($k \sim \frac{1}{L}h$/Mpc) the power spectrum starts to deviate significantly. However, in this regime the perturbations are already nonlinear and we cannot trust the results of the linear perturbation theory. Once we discuss the N-body results we will see that the symmetron mechanism is at work in this regime, thereby suppressing the predication of linear perturbation theory.

The relative short range of the fifth force means that it will not affect the CMB unless $L, \beta \gg 1$. Take $L = 1$ and $\beta = 2$ as an example: we find a maximal increase in power (due to the ISW effect) of $\sim 0.25\%$ for multipoles around $l \sim 100$. One needs a much larger β and/or L to have a detectable signature in the CMB. The second case is not allowed by local experiments while the first case implies a growth rate of the linear perturbations which should have difficulty satisfying constraints coming from large scale structure surveys.

A more thorough analysis of the linear perturbations in the symmetron model can be found in Brax et al. (2011b). There it was shown that strong signatures appears in other interesting linear observables such as the weak lensing slip parameter and the modified gravity parameter.

3.4. *Tachyonic Instability in the perturbations*

The perturbations in Sec. (3.2) were integrated using the approximate equation Eq. (39), which is equivalent to using the analytical minimum as the background field. The reason we did not use the full equations is because perturbations theory breaks down close to $z_{\rm SSB}$.

Immediately before $z_{\rm SSB}$ the field is still close to $\phi = 0$; as $z \to z_{\rm SSB}$ the mass of the field vanishes. This means that the field cannot follow the minimum and starts to lag behind as seen in Fig. (1). The global minimum of the effective potential $\phi = 0$ now becomes a local maximum and the mass squared of the field becomes negative leading to an exponential growth in the perturbations.

To see what happens we can simplify Eq. (37) by discarding all but the most important terms.

$$\ddot{\delta\phi} + \left(m_\phi^2 + \frac{k^2}{a^2}\right)\delta\phi \simeq 0 \tag{42}$$

If $m_\phi^2 + \frac{k^2}{a^2} < 0$ then the solution to the above equation reads $\delta\phi \propto e^{t\sqrt{|m_\phi^2 + k^2/a^2|}}$ which is exponentially growing.

In a realistic situation the field would roll very quickly down from the false minimum $\phi = 0$, making m_ϕ^2 positive, and thereby stabilizing the field close to the symmetry breaking minimum (Felder et al. 2001). Since perturbation theory is only valid as long as the perturbations $\delta\phi$ are small we get a breakdown of the perturbation theory when using the true background solution. The blow up in $\delta\phi$, in turn, leads to a blow up in the matter perturbations and the numerical results cannot be trusted.

We have investigated this further by using N-body simulations. In Fig. (10) we see a snapshot of the ϕ-distribution both before and after $z = z_{\rm SSB} = 2.0$. There we see the same sort of behavior as is familiar from symmetry breaking in condensed matter physics: symmetry breaking takes place at different places at different times according to the local matter density. This type of dynamics is not taken care of in the standard perturbation theory approach which leads to the apparent instability.

Note that by using the analytical minimum when integrating the perturbations we do not have control over the accuracy of our results. A full analysis of this phenomenon could be handled with N-body simulations, but in our simulations we have not explicitly taken into account the time variation of the scalar field (we work in the quasi-static limit) and our simulation box is also too small to reach far enough into the linear regime. We leave this study for future work.

3.5. *Varying Constants*

3.5.1. *WMAP constraints on particle mass variation*

One important constraint on coupled scalar field theories comes from time variation in the gravitational constant G in the Jordan frame, or equivalently in the masses of the standard model particles in the Einstein Frame. WMAP constrains any such variation to be less than about 5% since recombination (Nagata et al. 2004). Light element abundances provide similar constraints between the time of nucleosynthesis and today (Accetta et al. 1990).

Due to the conformal coupling to matter, $A(\phi)$, a constant mass scale in the Jordan frame becomes time and space varying in the Einstein frame. The mass

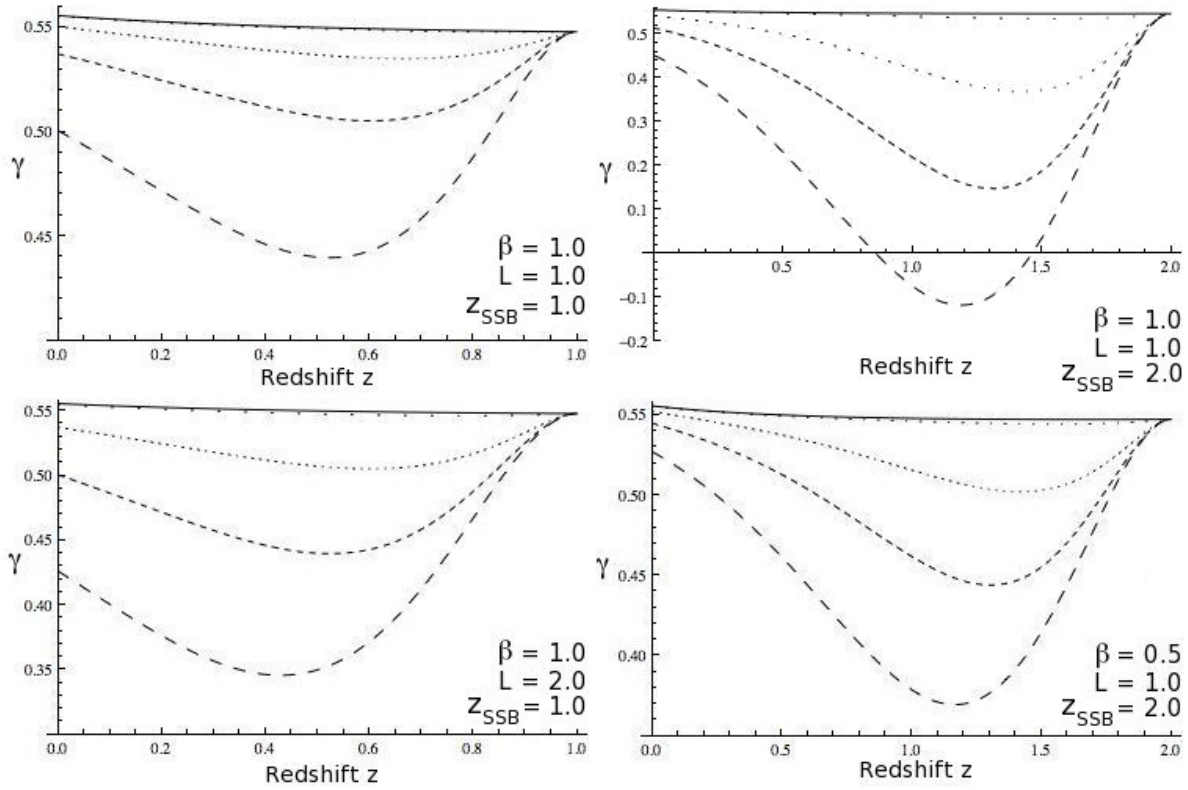

FIG. 2.— The evolution of the growth index $\gamma(z)$ when $z_{\rm SSB} = 1$ (left) and $z_{\rm SSB} = 2$ (right) for four different wavenumbers $k = \{0.01, 0.05, 0.1, 0.2\}$Mpc/h (from top to bottom in each figure). The solid line show the predication of ΛCDM.

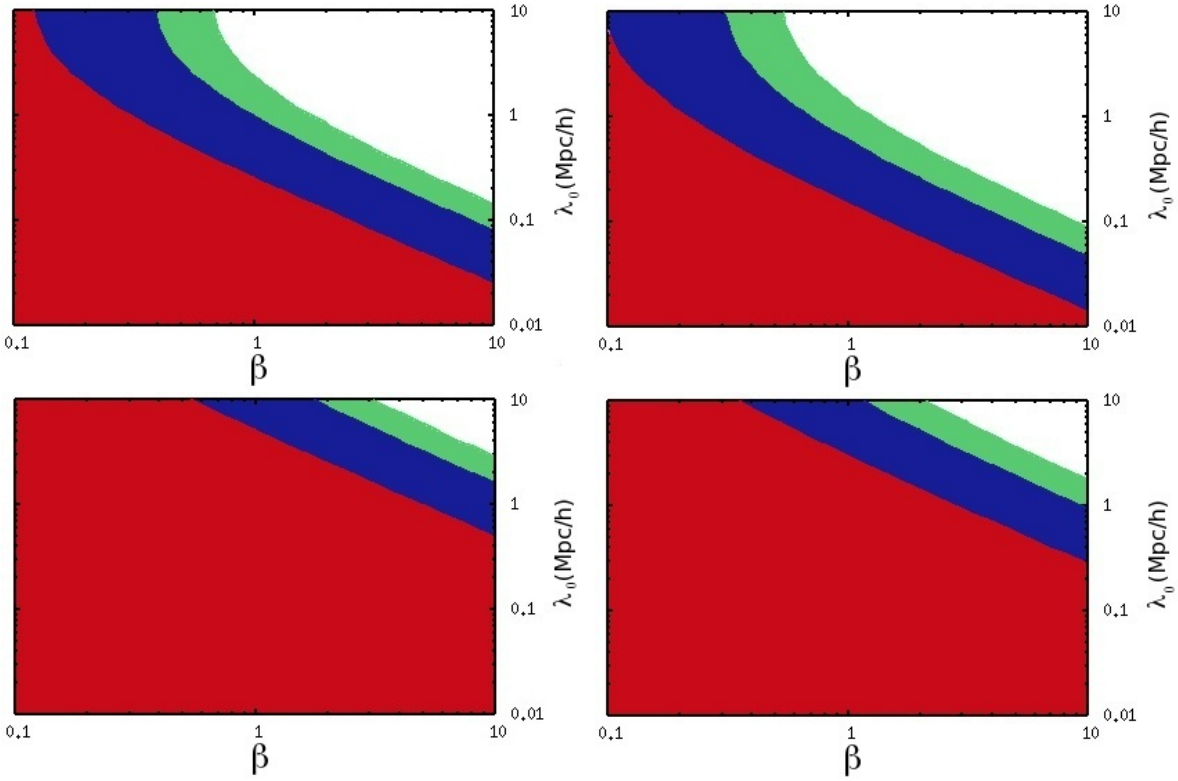

FIG. 3.— The growth index $\gamma(z = 0)$ for $z_{\rm SSB} = 1.0$ (left) and $z_{\rm SSB} = 2.0$ (right) for two comoving wavnumbers: $k = 0.2$Mpc/h (above) and $k = 0.01$Mpc/h (below). The red region shows the GR regime $\gamma \simeq 0.555$, the blue region show the regime where $0.5 < \gamma < 0.55$, the green region shows $0.4 < \gamma < 0.5$ and the white region shows $\gamma < 0.4$.

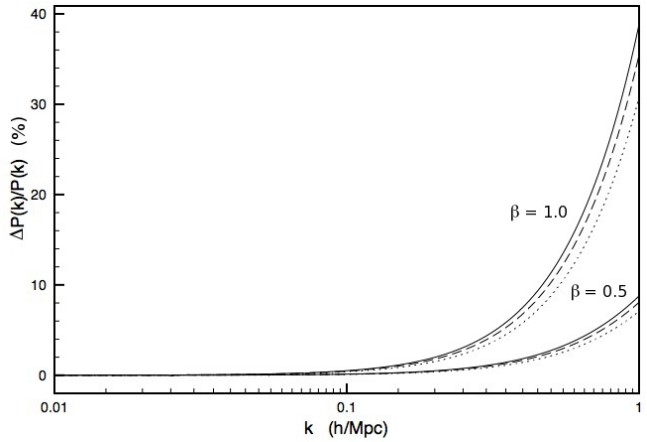

FIG. 4.— The linear power spectrum relative to that of ΛCDM for three different SSB redshifts: $z_{\rm SSB} = 0.5$ (dotted), $z_{\rm SSB} = 1.0$ (dashed) and $z_{\rm SSB} = 2.0$ (solid). We have fixed $L = 1$ and shown the results for the two values $\beta = 0.5$ and $\beta = 1.0$.

variation between today and recombination is given by

$$\frac{\Delta m}{m} = \frac{A(\phi_{\rm rec}) - A(\phi_{\rm today})}{A(\phi_{\rm rec})} \simeq \frac{1}{2}\left(\frac{\phi_{\rm today}}{M}\right)^2 \qquad (43)$$

where we have put $\phi_{\rm rec} \simeq 0$ since $z_{\rm rec} \gg z_{\rm SSB}$ in all interesting cases. If we further assume $\phi_{\rm today} = \phi_0$ we get the conservative constraint

$$\frac{\Delta m}{m} \simeq \frac{1}{2}\left(\frac{\phi_0}{M}\right)^2 = \beta^2\left(\frac{M}{M_{\rm pl}}\right)^2 < 10^{-6}\beta^2 \qquad (44)$$

The WMAP constraint $\left|\frac{\Delta m}{m}\right| \lesssim 0.05$ is satisfied for all $\beta \lesssim 100$.

3.5.2. *Fine structure constant*

Analysis of absorption spectra of quasars have led some to claim that the fine structure constant α might have evolved by approximately one part in 10^5 over the redshift range $0.2 < z < 3.7$. If this turns out to be true, then general covariance would imply that α can vary both in space and in time, that is, it must be a function of a field.

Since we have so far assumed that the symmetron couples conformally to matter fields, and since the Maxwell action is conformally invariant, at tree level the symmetron does not lead to a time varying α. By considering a coupling of the symmetron to photons of the form

$$S_\gamma = -\frac{1}{4}\int d^4x\sqrt{-g}A_\gamma(\phi)F_{\mu\nu}F^{\mu\nu} \qquad (45)$$

where

$$A_\gamma(\phi) = 1 + \frac{\zeta_\gamma}{2}\left(\frac{\phi}{M}\right)^2 \qquad (46)$$

then variations in ϕ will lead to variations in α. Here ζ_γ is the symmetron-photon coupling relative to the symmetron-matter coupling. The variation in the fine structure constant between Earth (E) and another place (S) in the Universe is given by

$$\left|\frac{\Delta\alpha}{\alpha}\right| = \frac{A_\gamma(\phi_E) - A_\gamma(\phi_S)}{A_\gamma(\phi_E)} \simeq \frac{\zeta_\gamma}{2}\left(\frac{\phi_S}{M}\right)^2 \qquad (47)$$

If S is a very low density environment where $\phi_S \approx \phi_0$ then

$$\left|\frac{\Delta\alpha}{\alpha}\right| \simeq \zeta_\gamma 10^{-6}\beta^2 \qquad (48)$$

which for $\mathcal{O}(1) \lesssim \beta, \zeta_\gamma$ is close to the reported detection.

However, the local density in most Ly-α emitting systems is usually much larger than the cosmological background density today (see e.g. Brax et al. (2004) and references therein), which implies $\phi_S \ll \phi_0$ and the above estimate becomes even smaller.

To be able to account for the reported claims we need $z_{\rm SSB}$ to be well before the observed redshift of these systems and/or these systems to be located in voids to produce the desired 10^{-5} effect. This makes it possible that the symmetron is responsible for the claimed variations, but most likely it will require a fine tuning $\zeta_\gamma \gg 1$. A more detailed analysis, as done in Li et al. (2011b), is required to see if this is the case. This is beyond the scope of this paper.

3.6. *N-body Equations*

To implement the general relativistic equations Eq. (5,12,13,16) in N-body simulations, it suffices to work in the nonrelativistic limits, since the simulations only probe the weak gravity regime and small volumes compared with the cosmos. We write the perturbed metric in the (flat) conformal Newtonian gauge as

$$ds^2 = -a^2(1+2\Xi)d\tau^2 + a^2(1-2\Psi)dx^\mu dx_\mu \qquad (49)$$

where τ is the conformal time and x^μ is the comoving coordinate.

The scalar field equation of motion in terms of the perturbed quantities becomes

$$\begin{aligned} &-(1-2\Xi)\phi'' + \nabla^2_{\mathbf{x}}\phi - \phi'\left(2H(1-2\Xi) - \Xi' - 3\Psi'\right) \\ &= a^2\left(\phi\left(\frac{\rho_m}{M^2} - \mu^2\right) + \lambda\phi^3\right) \end{aligned} \qquad (50)$$

Taking the quasi-static limit of this equation, in which we can neglect terms such as Ξ', Ψ' and $H\phi'$ since the time derivative of a quantity is much smaller than its spatial gradient, and removing the background part we obtain

$$\begin{aligned} \nabla^2_{\mathbf{x}}\phi \approx{}& \frac{a^2}{M^2_{\rm pl}}\left(\rho_m\phi - \overline{\rho}_m\overline{\phi}\right)\phi\Big) \\ &+ \frac{a^2}{M^2_{\rm pl}}\left(\mu^2(\overline{\phi} - \phi) + \lambda(\phi^3 - \overline{\phi}^3)\right) \end{aligned} \qquad (51)$$

where we have also used the approximation $A(\phi) \approx 1$ to simplify the equation further.

The $(0,0)$-component of the Ricci tensor and the trace of the total energy-momentum tensor in the perturbed quantities becomes

$$\begin{aligned} a^2R^0_0 \approx{}& -\nabla^2_{\mathbf{x}}\Xi + 3\left(\frac{a''}{a} - H^2\right)(1-2\Xi) \\ &- 3\Psi'' - 3H(\Xi' + \Psi') \end{aligned} \qquad (52)$$

$$T \approx -A(\phi)\rho_m - 4V(\phi) + \frac{1}{a^2}(1-2\Psi)\phi'^2 \qquad (53)$$

The $(0,0)$-component of the Einstein equation with the background part removed gives the nonrelativistic Poisson equation

$$\nabla^2_{\mathbf{x}}\Phi \approx 4\pi G\left(\rho_m - \overline{\rho}_m\right)a^3 \tag{54}$$

where we have neglected the contribution from the potential $(V(\phi) - V(\overline{\phi}))$, put $A(\phi) \approx 1$ and taken $\Phi = a\Xi$ for convenience.

The equation of motion for the N-body particles follows from the geodesic equation and reads

$$\ddot{\mathbf{x}} + 2H\dot{\mathbf{x}} = -\frac{1}{a^3}\nabla_{\mathbf{x}}\Phi - \frac{1}{a^2}\frac{\phi}{M^2}\nabla_{\mathbf{x}}\phi - \frac{\phi\dot{\phi}}{M^2}\dot{\mathbf{x}} \tag{55}$$

By rewriting this equation in terms of the conjugate momentum to $\mathbf{x}$, $\mathbf{p} = a^2\dot{\mathbf{x}}$, we have

$$\frac{d\mathbf{x}}{dt} = \frac{\mathbf{p}}{a^2} \tag{56}$$

$$\frac{d\mathbf{p}}{dt} = -\frac{1}{a}\nabla_{\mathbf{x}}\Phi - \frac{\phi}{M^2}\left(\nabla_{\mathbf{x}}\phi + \dot{\phi}\mathbf{p}\right) \tag{57}$$

The equations Eq. (51,54,56) are all we need to put into the N-body simulation code in order to study structure formation in the nonlinear regime.

4. N-BODY SIMULATIONS

Below we describe the algorithm and model specifications of the N-body simulations we have performed. We also give results from tests of the code to show that the scalar field solver works accurately.

4.1. *Outline*

For our simulations we have used a modified version of the publicly available N-body code MLAPM (Knebe et al. 2001). The modifications we have made follow the detailed prescription of Li & Barrow (2011a), and here we only give a brief description. The MLAPM code has two sets of meshes: the first includes a series of increasingly refined regular meshes covering the whole cubic simulation box, with respectively 4,8,16,...,N_d cells on each side, where N_d is the size of the domain grid, which is the most refined of these regular meshes. This set of meshes are needed to solve the Poisson equation using multigrid method or fast Fourier transform (for the latter only the domain grid is necessary). When the particle density in a cell exceeds a pre-defined threshold, the cell is further refined into eight equally sized cubic cells; the refinement is done on a cell by cell basis and the resulting refinement could have arbitrary shape which matches the true equal density contours of the matter distribution. This second set of meshes are used to solve the Poisson equation using the linear Gauss-Seidel relaxation scheme.

The symmetron field is the most important ingredient in the model studied here, and we have to solve for it to obtain detailed information about the fifth force. In our N-body code, we have added a new scalar field solver. It uses a nonlinear Gauss-Seidel scheme for the relaxation iteration and the same criterion for convergence as the default Poisson solver in MLAPM. But it uses V-cycle instead of the self-adaptive scheme in arranging the Gauss-Seidel iterations.

The modified Poisson equation is then solved using nonlinear Gauss-Seidel relaxation on both the domain grid and the refinements. With the gravitational potential Φ and the scalar field ϕ at hand, we can evaluate the total force on the particles and update their momenta/velocities which are used to advance the particles in space.

4.2. *Simulation Details*

The physical parameters we use in the simulations are as follows: the present dark-energy fractional energy density $\Omega_\Lambda = 0.733$ and $\Omega_m = 0.267$, $H_0 = 71.9\mathrm{km}/s/\mathrm{Mpc}$, $n_s = 0.963$ and $\sigma_8 = 0.801$. We use a simulation box with size $64\mathrm{Mpc}/h$, in which $h = H_0/(100\mathrm{km}/s/\mathrm{Mpc})$. We simulate 9 different models, see Table. (1) for the symmetron parameter values.

These parameters are chosen so that they predict local fifth forces which are of the same order of magnitude as allowed by current experiments and observations and are such that we can see the effect of the different parameters. Note that the energy density in the symmetron is always much less than that of dark energy and therefore does not alter the background cosmology which in all runs will be that of ΛCDM.

In all those simulations, the particle number is 256^3, so that the mass resolution is $1.114 \times 10^9\mathrm{Mpc}/h$. The domain grid is a $128 \times 128 \times 128$ cubic and the finest refined grids have 16384 cells on each side, corresponding to a force resolution of about $12\mathrm{kpc}/h$. The force resolution determines the smallest scale on which the numerical results are reliable. Our simulations are purely N-body, which means that baryonic physics has not been included in the numerical code.

4.3. *Initial conditions*

Initial conditions for the simulation was generated using GRAFIC2 (Bertschinger 2001; Prunet et al. 2008) by using the parameters described above, but where we also included baryons with a density parameter $\Omega_b = 0.045$ (and a dark matter density $\Omega_m = 0.267 - \Omega_b$). We use the same initial conditions for all the simulations in order to see clearly the effect of the symmetron compared with ΛCDM.

This choice needs some justification. First of all, we start the simulation at $z = 49$, a time in which the symmetron has no effect on the growth of the perturbations. This means that the only change the symmetron will have on the initial conditions is on the value of σ_8 today which is used to normalize the perturbations. Since the symmetron field has a rather short range compared to the linear regime we do not expect a large effect on σ_8 for the range $L \lesssim \mathcal{O}(1)$ we are considering.

To check this assumption we integrated the perturbations and calculated the value of σ_8 (by normalizing to the CMB) for our simulation models and found that the model with $L = 1$ that is furthest away from ΛCDM, namely F in which $z_{\mathrm{SSB}} = 2.0$, $L = 1$ and $\beta = 1$, only has $\sigma_8 \simeq 1.01\sigma_8^{\mathrm{LCDM}}$ justifying the use of ΛCDM initial conditions.

If one is to consider models in which L is much larger than 1 then this becomes an issue that should be dealt with properly.

4.4. *Code tests*

Model:	**A**	**B**	**C**	**D**	**E**	**F**	**G**	**H**	**ΛCDM**
$z_{\rm SSB}$	0.5	0.5	1.0	1.0	2.0	2.0	1.0	1.0	0.0
β	0.5	1.0	0.5	1.0	0.5	1.0	0.5	1.0	0.0
L	1.0	1.0	1.0	1.0	1.0	1.0	2.0	2.0	0.0

TABLE 1
The symmetron parameters used in our simulations.

Before we run simulations we have to make sure that the scalar field solver, which is the main modification to the MLAPM code, works accurately by performing code tests for situations where the outcome is known from analytical solutions.

The scalar field solver uses the nonlinear Newton-Gauss-Seidel relaxation scheme to compute $\chi \equiv \frac{\phi}{\phi_0}$, and an indicator that it works is to show that, given the initial guess of the solution that is very different from the true solution, the relaxation could produce the latter within a reasonable number of iterations. We consider a simulation box with homogeneous density (obtained by putting particles on a regular grid inside the simulation box), then the true solution is given by $\chi = \overline{\chi}$: the background solution. We therefore make an initial guess for χ which is randomly scattered around $\overline{\chi}$ and let the scalar field solver solve for χ. The results for $|\chi - \overline{\chi}|$ before and after the relaxation scheme are shown in Fig. (5). The differences between the initial guess and the true solution varies between 0.001 and 0.1 while after the relaxation the difference is of order 10^{-8}. By using double precision numbers in all the calculations we obtained exactly the analytical solution (to double precision $\approx 10^{-15}$), while for using only floating point numbers the accuracy dropped to 10^{-6} which is exactly the accuracy in floats. This shows that the scalar field solver works accurately.

The most important effect of the symmetron is the screening mechanism in which the local value of the field should be pushed down towards $\chi = 0$ in high density environments. We therefore consider a spherical over-density, located at the center of the box, with a given radius R, homogeneous density ρ_c inside R and embedded in a background of homogenous density ρ_b. The analytical solution reads

$$\chi(r) = \chi(0)\frac{\sinh[m_c r]}{m_c r}, \qquad r < R \quad (58)$$

$$\chi(r) = \chi_b + \frac{(\chi(R) - \chi_b)R}{r} e^{-m_b(r-R)}, \qquad r > R \quad (59)$$

where

$$m_c^2 \simeq \left(\frac{\rho_c}{M^2}\right), \quad m_b^2 \simeq \left(\frac{\rho_b}{M^2} + \mu^2(3\chi_b^2 - 1)\right)$$

$$\chi_b \simeq \sqrt{1 - \frac{\rho_b}{\rho_{\rm SSB}}}, \quad \chi(R) = \chi_b \left(\frac{1 + m_b R}{\frac{m_c R}{\sinh(m_c R)} + m_b R}\right)$$

$$\chi(0) = \chi_b \left(\frac{1 + m_b R}{1 + \frac{\sinh(m_c R)}{m_c R} m_b R}\right). \quad (60)$$

For the trial solution on the grid we use the background value χ_b and we perform the test for a range of densities ρ_c. The results after relaxation for the most massive cases are shown in Fig. (6). There are some small discrepancy from the analytical solution in the region $R < r < 2R$ for the most extreme cases $\rho_c > 10^3 \rho_b$. This is not a surprise as the density suddenly drops over 3 orders of magnitude at $r = R$, meaning that we need a lot of particles in this region in order to get accurate results. In the region $r < R$ and $r > 2R$ the scalar field solver produces the analytical solution to high accuracy.

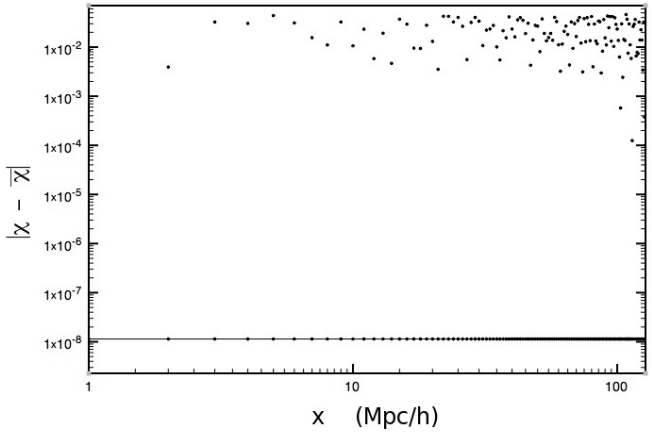

Fig. 5.— The scalar field relative to the analytical solution before (random initial values above) and after (below) the Newton-Gauss-Seidel relaxation.

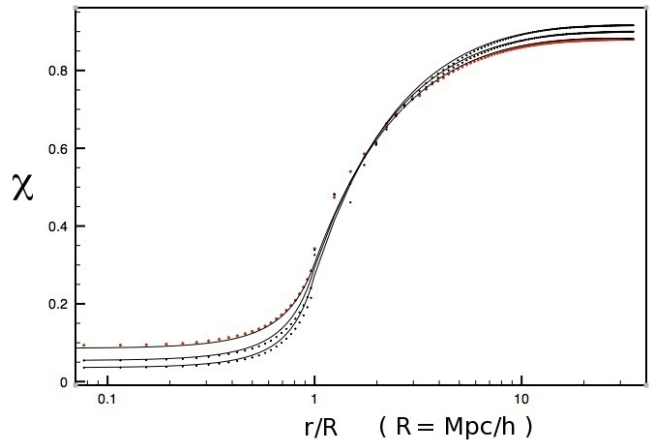

Fig. 6.— The scalar field value as function as distance from the center for a spherical over-density embedded in a background of homogenous density ρ_b together with the analytical solution for $\rho_c = 4000$, 6000 and 8000 times ρ_b. The points shown here are calculated by binning the scalar field value using a bin-width $\Delta(r/R) = 0.01$ and taking the average. We used the same amount of particles, 128^3, in each run so that the background density ρ_b differs for the three cases shown above.

5. NUMERICAL RESULTS

In this section we present the results from the simulations, including the snapshots, the matter power spectrum and the halo mass function.

5.1. *Snapshots*

In the symmetron model $\chi = \frac{\phi}{\phi_0}$, and thereby the fifth force, is suppressed in high density regions. In this subsection we demonstrate these qualitative features using some snapshots.

Fig. (7) shows the ratio of the fifth force to gravity today for redshift both before and after $z_{\rm SSB}$.

At early times, the density is high everywhere and we expect the fifth force on all particles to be strongly suppressed. At later times we expect a screening in regions of high matter density. These predictions are confirmed in Fig. (7). We see that fifth force on the particles which feel a strong gravitational force (i.e. particles in a high density environment) is highly suppressed whereas the fifth force on particles which feel a weak gravitational force (i.e. particles in a low density environment) follows the unscreened theoretical prediction $F_\phi \simeq 2\beta^2\chi_b^2(z)F_{\rm gravity}$ (see Eq. (39)).

Fig. (8)-(10) shows the density and scalar field distribution in a slice of the simulation box at different redshifts for the three cases $z_{\rm SSB} = 0.5, 1.0$ and 2.0 with $\beta = L = 1.0$ fixed.

For redshifts $z > z_{\rm SSB}$, χ is very close to the minimum $\chi = 0$ almost everywhere in space except in voids where the symmetry has already been (weakly) broken. When we go down to redshifts $z < z_{\rm SSB}$ the symmetry is broken in most parts of the box, except in the high density regions where we still have $\chi \sim 0$. Comparing the scalar field distribution today for runs with different $z_{\rm SSB}$, we see that the earlier the symmetry breaking takes place the larger the part of the box which is unscreened ($\chi \sim 1$) today becomes. This is because the critical density for the symmetry breaking is larger for larger $z_{\rm SSB}$ and therefore the halos have to be more massive in order to be effectively screened.

5.2. *Matter power spectrum*

The nonlinear matter power spectrum is an important observable and could be used to distinguish among different models of structure formation. As we have seen above the symmetron can have a strong effect on the growth rate of the linear perturbations for parameters that are allowed by local experiments. We expect these signatures to show up in the nonlinear matter power spectrum.

Fig. (12) displays the fractional difference in the matter power spectrum from that of ΛCDM, defined as $(P(k) - P_{\Lambda CDM}(k))/P(k)$, and in Fig. (11) we show the actual power spectrums for the symmetron and ΛCDM together with the corresponding predictions from linear perturbations theory.

The power spectrum agrees with the predictions of linear perturbation theory on large scales ($k \lesssim 0.1$ Mpc$/h$), but on smaller scales the results found here are weaker than the prediction of linear perturbation theory seen in Fig. (4). This is because when linearizing the field equation we are basically using the background matter density everywhere and therefore preventing the symmetron mechanism to take effect in suppressing the fifth force when matter perturbations become large. In contrast, the N-body simulation avoids this approximation by taking full account of the suppression of the fifth force.

The fractional difference relative to ΛCDM is growing with $z_{\rm SSB}$ and β as the fifth force has more time to operate and is stronger. Comparing runs with the same β we see an important effect if the symmetry breaking is earlier. When $z_{\rm SSB} = 2.0$ the fractional power is increasing until we reach a scale where the screening mechanism becomes stronger and then starts to decrease again towards ΛCDM, only to start growing again at even smaller scales. This is because the critical density for having screening is much higher for larger $z_{\rm SSB}$ so that most halos (which are on small scales and of low mass) are unscreened.

In Fig. (13) we show the redshift evolution of the power spectrum. The power spectrum is found to be practically identical to that of ΛCDM for redshifts $z > z_{\rm SSB}$, but as soon as the symmetry breaks at the background level, the symmetron fifth force can kick in and enhance the clustering of matter.

It is clear from Fig. (12) that there exist a large range of parameters in which the symmetron model can be easily distinguished from ΛCDM.

5.3. *Halo profiles for χ*

In Fig. (14) we show the profile of χ inside the most massive halos found in the simulation. Since the fifth force is proportional to χ this figure also provides information about the fifth force in halos.

The field profile of χ is seen to increase from the inner to the outer regions of the halos and shows that the fifth force is most suppressed in the central region as expected.

The fifth force is stronger for smaller halos, because those generally reside in low density regions where the fifth force is less suppressed. We see the closer the symmetry breaking redshift is to 0, the smaller χ becomes inside the halo and the more suppressed the fifth force is. Again this is because early symmetry breaking means a higher critical density and halo needs to be more massive to be effectively screened. This effect is also seen in Fig. (8,9,10) (notice the difference in distribution of χ at $z = 0$ between the different runs) and also on the matter power spectrum in Fig. (12) (notice the way the power spectrum starts growing again on small scales for $z_{\rm SSB} = 2.0$).

This has some important consequences for the local constraints. We mentioned in Sec. (2.1) that the local constraints were derived by assuming that our galactic neighborhood was not screened today, and lead to the constraint

$$L(1 + z_{\rm SSB})^{3/2} \lesssim 2.3, \tag{61}$$

From our numerical results we see that when $z_{\rm SSB} = 2.0$ its only the most massive halos that are screened. This means that the assumption that went into the constraint above is very likely to be true. On the other hand for SSB that happens very close to today, halos of much smaller mass are in fact screened and it might be possible to have a range L that exceeds Eq. (61) and still be in agreement with experiments.

We note that we have not seen any significant effect on the halo density profiles. For a given mass range, the halo profiles seem to have approximately the same distribution. There should be some important differences for low mass halos, but the resolution in our simulation is too low to study this.

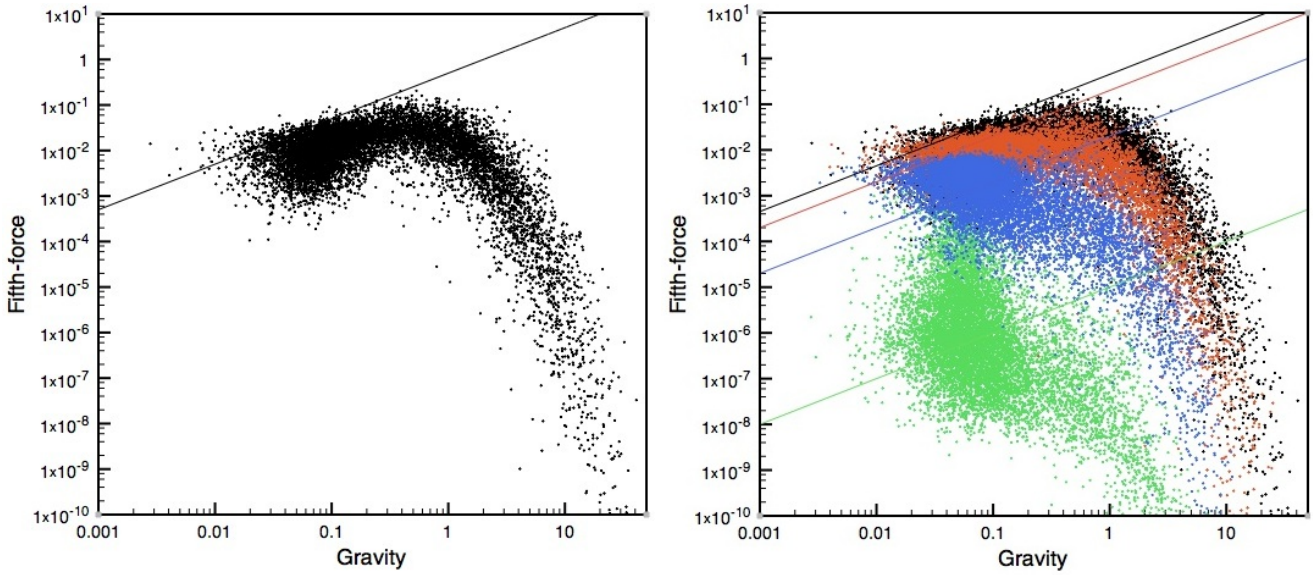

FIG. 7.— The fifth force to gravity for in a slice of the simulation box at $z = 0$ (left) and the comparison between four different redshift (right) for a runs with $z_{\rm SSB} = 0.5$, $\beta = 1$ and $L = 1$. Black shows $z = 0$, red $z = 0.25$, blue $z = 0.65$ and green $z = 1$. The solid lines shows $\frac{F_\phi}{F_{\rm gravity}} = 2\beta^2\chi_b^2(z)$ which is the prediction for the (short-range) forces at the perturbation level (see Eq. (39)). Note that the force will be dispersed around this prediction because we already have significant over and under densities in which $\chi \neq \chi_b$. At $z = 1$ the background field is close to $\chi_b = 0$ and the force is small everywhere in space. As we move closer to $z = 0$, the symmetry breaks, and the background value moves towards $\chi_b = 1$. This means that the force in low density regions (small gravitational force) will increase whereas in high density regions (strong gravitational force) the screening kicks in and the force becomes suppressed just as seen above. The numerical size of the forces are given in terms of code units which are $\frac{H_0^2}{B}$ times the physical force unit.

However, the halo number counts was significantly different as we shall see in the next section.

5.4. *Halo mass function*

The halo mass function n is another key structure formation observable. It is defined to be the number density of dark matter halos within a given mass range. Because of the symmetron fifth force we expect more halos to be formed relative to the standard ΛCDM scenario.

We first look at the total number of halos (the integrated mass function) with more than 100 particles which clearly shows the effect of the fifth force, see Table. (2).

In Fig. (15) we have shown the mass function of the symmetron compared to ΛCDM at $z = 0$. We see a significantly higher mass function, especially for low mass halos which are generally found in low density regions where the fifth force is unscreened. The earlier symmetry breaking occurs and the stronger the coupling strength β, the more halos are formed in agreement to what we would naively expect.

The mass function converges to that of ΛCDM at very large halo masses for most parameters we have looked at. This is because the most massive halos have taken a very long time to form and therefore when the symmetron kicks in at some low redshift the halo is already massive enough to be screened. However, for the largest $z_{\rm SSB} = 2.0$ we do have small increases in both the halo number density and the mass of the most massive halos. There have been reports of some tension between observations and ΛCDM predictions with regards to very massive halos. Unfortunately for the symmetron model to be able to elevate this tension significantly we would need values of the parameters which are in conflict with local experiments.

There is a large range of viable parameters for the symmetron where the mass function deviates significantly from ΛCDM.

6. SUMMARY AND CONCLUSIONS

The symmetron mechanism is one way a scalar field can be non-minimally coupled to matter and still evade local gravity experiments. The symmetron model suffers the same fine tuning problems as chameleon models, but has the advantage of looking like a more natural effective theory.

The energy density of the symmetron is too low to contribute to the dark energy and we must therefore add a cosmological constant to get accelerated expansion of the Universe. The background evolution of the symmetron model is simply indistinguishable from that of the ΛCDM model.

This degeneracy is broken by the linear perturbations. In particular we have shown that the linear growth index $\gamma(z, k)$ can have a significant scale and redshift dependence together with a value today which can be distinguished from the ΛCDM prediction for a large part of the parameter space.

The structure formation in the nonlinear regime was investigated by using N-body simulations. N-body simulations have the advantage over linear theory in its ability of fully capturing the nonlinear environmental dependence of the symmetron field. Our results confirm the expectation that in high density environments the fifth force becomes screened. Consequently, the key observables such as the nonlinear matter power spectrum is closer to the ΛCDM predictions that expected from a linear analysis.

We found that the symmetron can still produce large

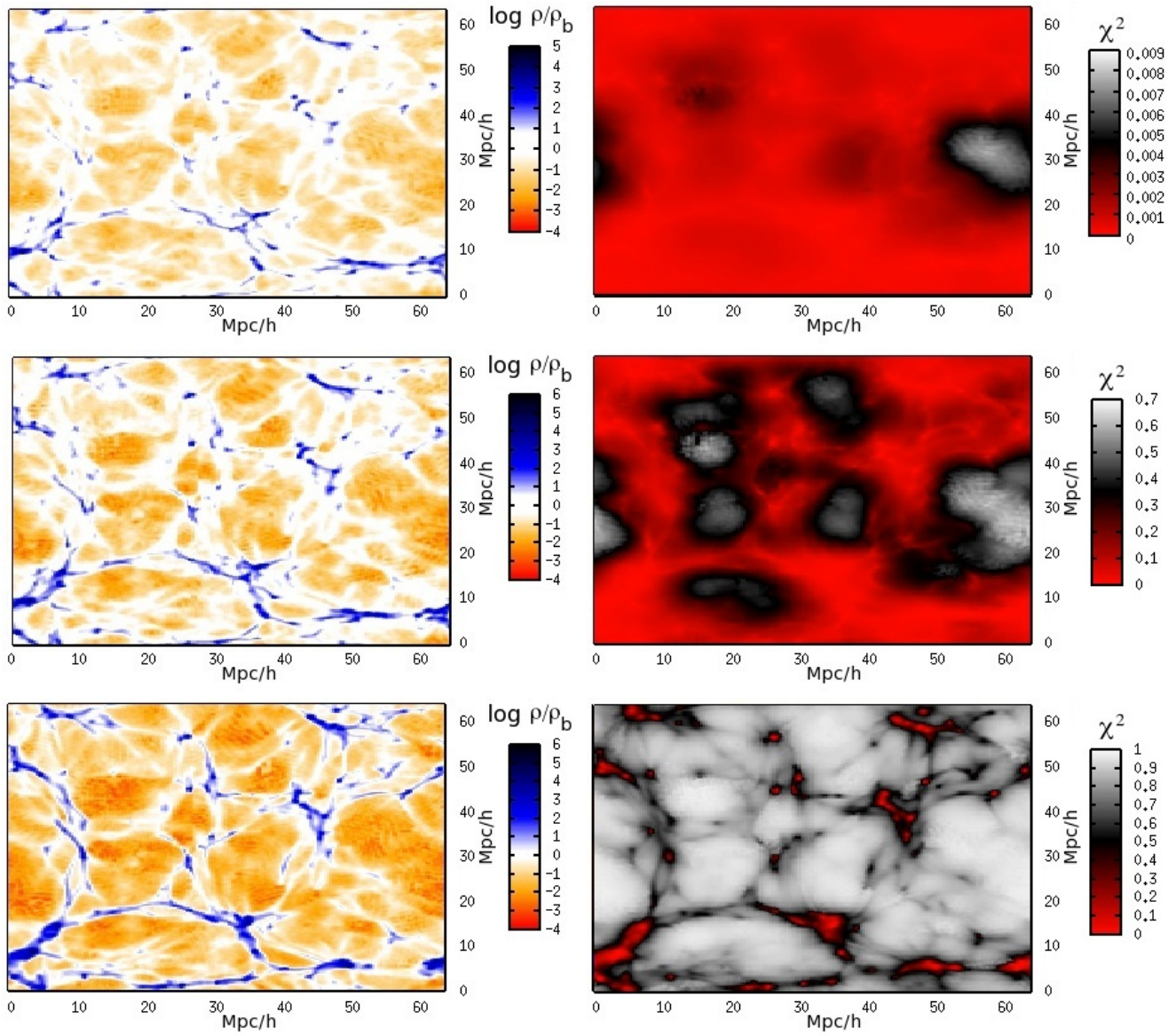

FIG. 8.— The density distribution (left) and scalar-field distribution (right) for a run with $z_{\rm SSB} = 0.5$, $\beta = 1$ and $L = 1$. From top to bottom $z = 1$, $z = 0.66$ and $z = 0$.

A	B	C	D	E	F	G	H	ΛCDM
1634	1694	1678	1871	1758	2051	1671	1788	1607

TABLE 2
THE HALO COUNT FOR OUR NINE SIMULATIONS. THE CORRESPONDING SYMMETRON PARAMETERS CAN BE FOUND IN TABLE. (1).

observable signatures in both the nonlinear matter power spectrum and the halo mass function, which could in principle be detected by current and near future cosmological observations such as Euclid.

Note that in the simulations performed in this work, we have treated baryons as dark matter. However, since the symmetron field has a uniform coupling to all matter fields we expect that all the results will qualitatively remain even after baryons are included.

In conclusion, the symmetron model has been found to have a wide range of observable cosmological effects on both linear and nonlinear scales. This adds to the list of observational signatures like making galaxies brighter (Davis et al. 2011) and the possibility of being detected in near future local gravity experiments (Hinterbichler & Khoury 2010) to mention some. The symmetron is therefore a good candidate for the detection of new physics beyond the standard model.

ACKNOWLEDGMENTS

The work described in this paper has been performed on TITAN, the computing facilities at the University of Oslo in Norway. The matter power spectrum was computed using POWMES (Colombi et al. 2009)

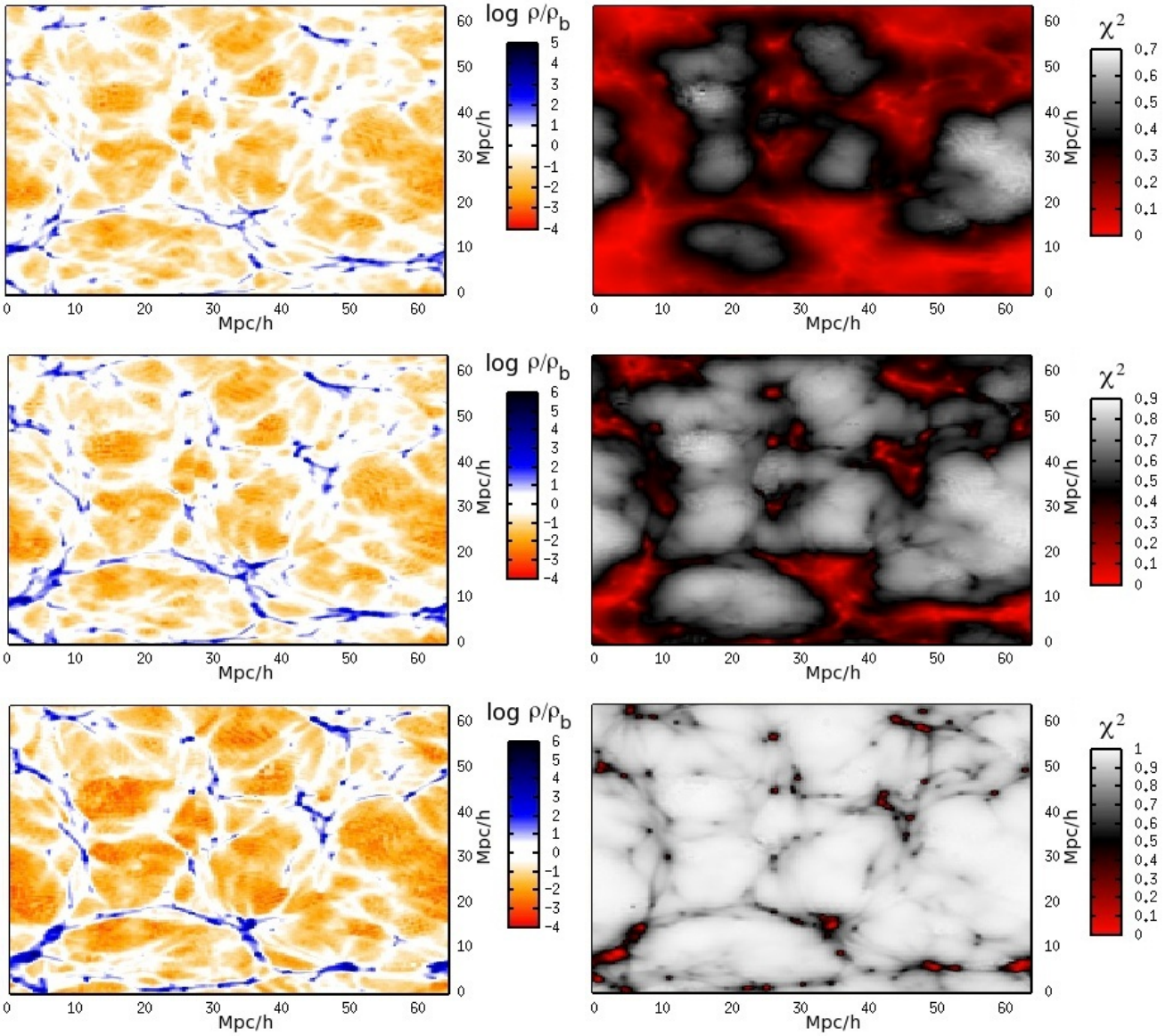

FIG. 9.— The density distribution (left) and scalar-field distribution (right) for a run with $z_{\rm SSB} = 1$, $\beta = 1$ and $L = 1$. From top to bottom $z = 1$, $z = 0.66$ and $z = 0$.

and the halo properties using MHF (Gill et al. 2004). D.F.M. and H.A.W. thanks the Research Council of Norway FRINAT grant 197251/V30. D.F.M. is also partially supported by project PTDC/FIS/111725/2009 and CERN/FP/123618/2011. H.A.W. thanks DAMPT at Cambridge University for the hospitality where a part of this work was carried out. B.L. is supported by Queens' College and the Department of Applied Maths and Theoretical Physics of University of Cambridge. B.L. and A.C.D. thank STFC for partial support. We would also like to thank Douglas Shaw for useful discussions.

APPENDIX A: USEFUL EXPRESSIONS

Up to first order in the perturbed metric variables Ξ, Ψ the non-zero components of the symmetric Levi-Civita connection are

$$\Gamma^0_{00} = \frac{a'}{a} + \Xi' \tag{62}$$

$$\Gamma^0_{0k} = \Xi_{,k} \tag{63}$$

$$\Gamma^i_{00} = \Xi^{,i} \tag{64}$$

$$\Gamma^i_{0k} = \left(\frac{a'}{a} - \Psi'\right)\delta^i_k \tag{65}$$

$$\Gamma^0_{jk} = \delta_{jk}\left(\frac{a'}{a}(1 - 2\Xi - 2\Psi) - \Psi'\right) \tag{66}$$

$$\Gamma^i_{jk} = -\Psi_{,k}\delta^i_j - \Psi_{,j}\delta^i_k + \Psi^i_{,}\delta_{jk} \tag{67}$$

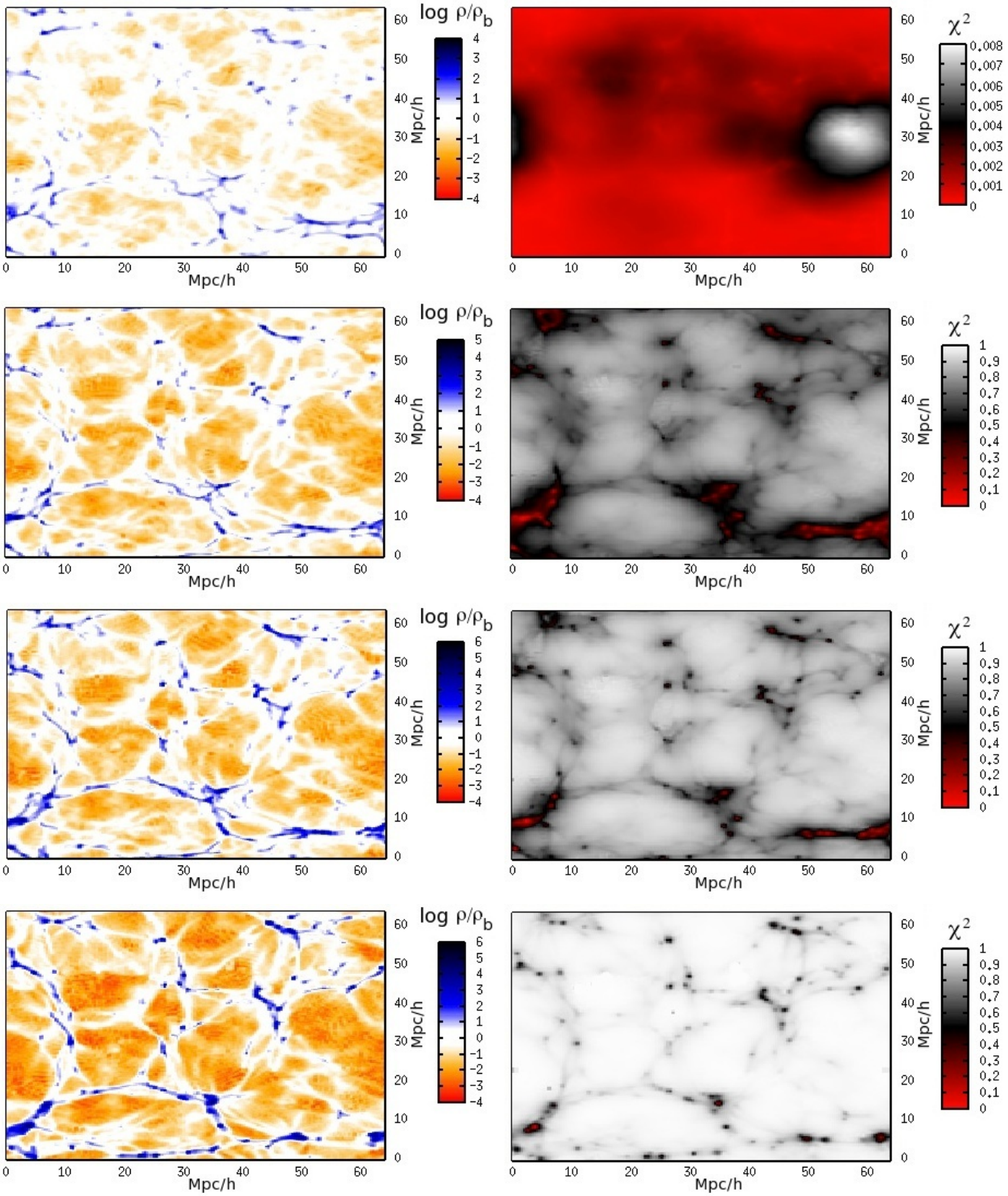

FIG. 10.— The density distribution (left) and scalar-field distribution (right) for a run with $z_{\rm SSB} = 2$, $\beta = 1$ and $L = 1$. From top to bottom $z = 2.33$, $z = 1$, $z = 0.66$ and $z = 0$.

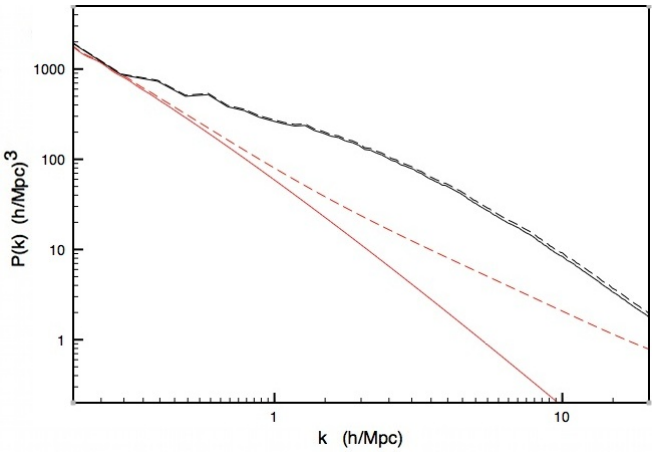

FIG. 11.— The full nonlinear power spectrum for a run with $z_{\rm SSB} = L = \beta = 1.0$ (dashed black) and ΛCDM (solid black). For comparison we also show the corresponding predications from linear perturbations theory in red. We clearly see the effectiveness of the screening mechanism. The linear predications do not take the symmetron mechanism into account and are hugely overestimating the power on small scales relative to ΛCDM.

From these expression we find that the components of the Ricci tensor and Ricci scalar are found to be

$$R_{00} = \Xi^{,i}_{,i} - 3\left(\frac{a''}{a} - \left(\frac{a'}{a}\right)^2\right) + 3\Psi'' + 3\frac{a'}{a}(\Psi' + \Xi') \tag{68}$$

$$R_{0j} = 2\Psi'_{,j} + 2\frac{a'}{a}\Xi_{,j} \tag{69}$$

$$R_{ij} = -\Psi''\delta_{ij} - \frac{a'}{a}(\Xi' + 5\Psi')\delta_{ij} - \Psi^{,k}_{,k}\delta_{ij} + \left(\frac{a''}{a} + \left(\frac{a'}{a}\right)^2\right)(1 - 2\Psi - 2\Xi)\delta_{ij} - (\Xi - \Psi)_{,ij} \tag{70}$$

$$R = 6\frac{a''}{a^3}(1 - 2\Xi) + \frac{1}{a^2}(4\Psi^{,k}_{,k} - \Xi^{,k}_{,k}) - \frac{6}{a^2}\left(\Psi'' + \frac{a'}{a}(\Xi' + 3\Psi')\right) \tag{71}$$

APPENDIX B: DISCRETISATION OF EQUATIONS

To implement the nonrelativistic equations into our numerical code, we have to rewrite then using code units, which are given by

$$\mathbf{x_c} = \frac{\mathbf{x}}{B}, \quad \mathbf{p_c} = \frac{\mathbf{p}}{H_0 B}, \quad t_c = tH_0, \quad \chi = \frac{\phi}{\phi_0}$$
$$\mathbf{\Phi_c} = \frac{\mathbf{\Phi}}{(H_0 B)^2}, \quad \rho_{\mathbf{c}} = \frac{\rho_{\mathbf{m}}}{\overline{\rho_{\mathbf{m}}}}, \quad \nabla = \mathbf{B}\nabla_{\mathbf{x}} \tag{72}$$

where subscript $_c$ stands for code units, B is the boxsize, $H_0 = 100{\rm km}/s/{\rm Mpc}$ and an overline denotes background quantities. In what follows we shall write $\nabla = \nabla_c$ for simplicity.

6.1. *Scalar field equation of motion*

The equation of motion for χ in code units becomes

$$\frac{ac^2}{(BH_0)^2}\nabla^2\chi \simeq a^3\left(\overline{\chi} - \chi + \chi^3 - \overline{\chi}^3\right)\left(\frac{\mu}{H_0}\right)^2 + 3\Omega_m\left(\frac{M_{\rm pl}}{M}\right)^2(\rho_c\chi - \overline{\chi}) \tag{73}$$

where $\overline{\chi}$ is the background solutions and we have used $\phi_0^2 = \frac{\mu^2}{\lambda}$ to simplify. Note that χ varies in the region $0 \leq \chi^2 \leq 1$. Discreticed this equation becomes $L^h(\chi_{i,j,k}) = 0$ where

$$\begin{aligned} L^h(\chi_{i,j,k}) = {} & \frac{1}{h^2}\frac{ac^2}{(BH_0)^2}\left(\chi_{i+1,j,k} - 2\chi_{i,j,k} + \chi_{i-1,j,k}\right) \\ & + \frac{1}{h^2}\frac{ac^2}{(BH_0)^2}\left(\chi_{i,j+1,k} - 2\chi_{i,j,k} + \chi_{i,j-1,k}\right) \\ & + \frac{1}{h^2}\frac{ac^2}{(BH_0)^2}\left(\chi_{i,j,k+1} - 2\chi_{i,j,k} + \chi_{i,j,k-1}\right) \\ & - a^3\left(\frac{\mu}{H_0}\right)^2(\overline{\chi} - \chi_{i,j,k}) \times \\ & \times\left(1 - \chi^2_{i,j,k} - \overline{\chi}\chi_{i,j,k} - \overline{\chi}^2\right) \\ & - 3\Omega_m\left(\frac{M_{\rm pl}}{M}\right)^2(\rho_c\chi_{i,j,k} - \overline{\chi}) \end{aligned} \tag{74}$$

The Newton-Gauss-Seidel iteration says that we can obtain a new and more accurate solution of $\chi^{\rm new}_{i,j,k}$ using our knowledge about the old solution $\chi^{\rm old}_{i,j,k}$ as

$$\chi^{\rm new}_{i,j,k} = \chi^{\rm old}_{i,j,k} - \frac{L^h(\chi^{\rm old}_{i,j,k})}{\partial L^h(\chi^{\rm old}_{i,j,k})/\partial\chi^{\rm old}_{i,j,k}} \tag{75}$$

where

$$\frac{\partial L^h(\chi_{i,j,k})}{\partial\chi_{i,j,k}} = -\frac{6}{h^2}\frac{ac^2}{(BH_0)^2} + a^3\left(\frac{\mu}{H_0}\right)^2\left(1 - 3\chi^2_{i,j,k}\right) - 3\Omega_m\left(\frac{M_{\rm pl}}{M}\right)^2\rho_c \tag{76}$$

6.2. *Poisson Equation*

Since we can neglect the scalar field contribution to the Poisson equation, it remains unmodified from that of ΛCDM and reads (in code units)

$$\nabla^2\Phi_c = \frac{3}{2}\Omega_m(\rho_{c,i,j,k} - 1) \tag{77}$$

6.3. *Particle equation of motion*

Using the code units, Eq. (56) can be rewritten as

$$\frac{d\mathbf{x_c}}{dt_c} = \frac{\mathbf{p_c}}{a^2} \tag{78}$$

$$\frac{d\mathbf{p_c}}{dt_c} = -\frac{1}{a}\nabla\Phi_c - \chi\left(\frac{\beta M}{M_{\rm pl}}\right)^2\left(\frac{c^2\nabla\chi}{(BH_0)^2} + \frac{d\chi}{dt_c}\mathbf{p_c}\right) \tag{79}$$

The factor $\left(\frac{M}{M_{\rm pl}}\right)^2$ can be also rewritten in terms of L, β and $z_{\rm SSB}$ by using Eq. (22).

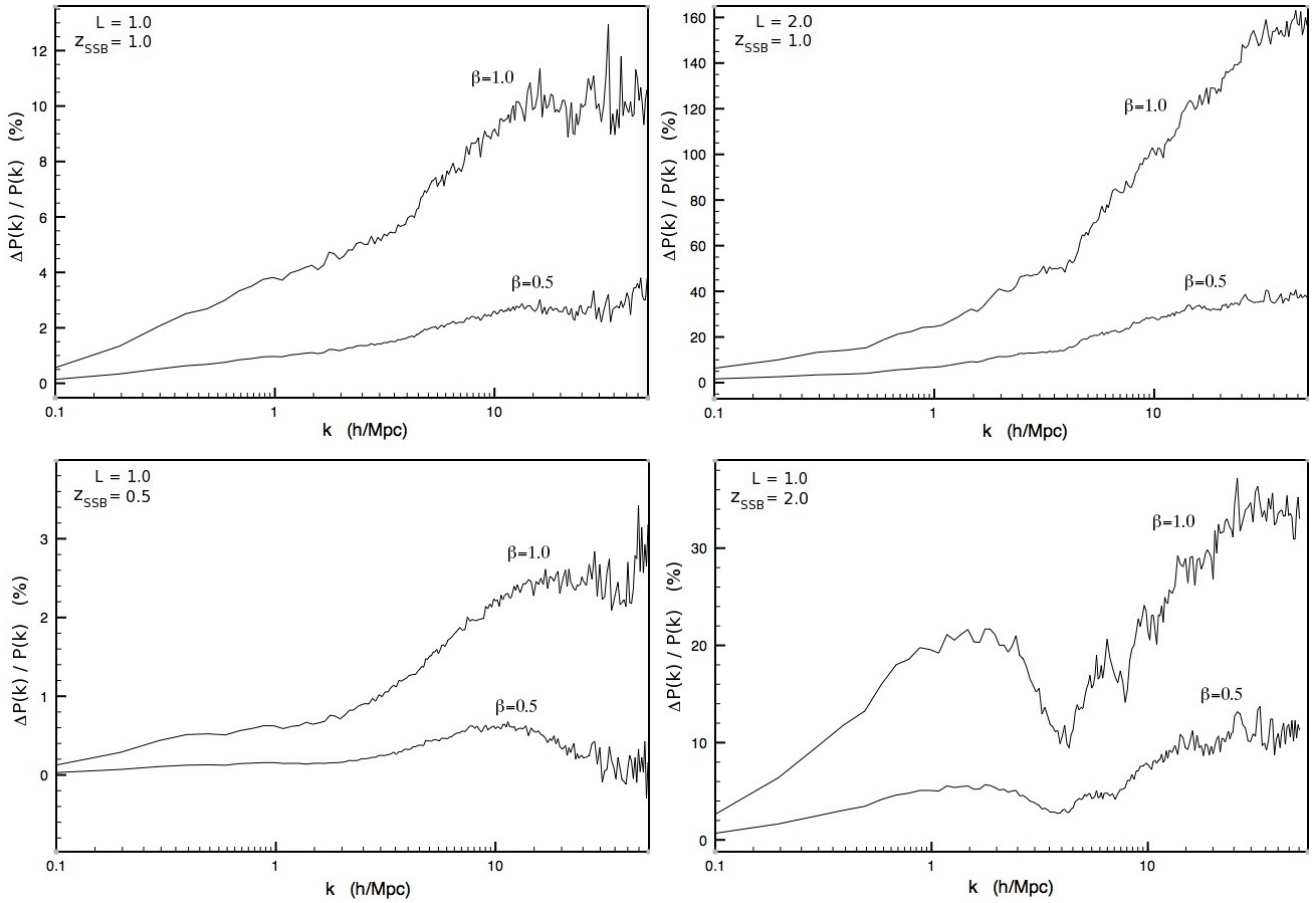

FIG. 12.— The fractional difference in the nonlinear power spectrum relative to ΛCDM for $\{z_{\rm SSB} = 1.0, L = 1.0\}$ (top left), $\{z_{\rm SSB} = 1.0, L = 2.0\}$ (top right), $\{z_{\rm SSB} = 0.5, L = 1.0\}$ (bottom left) and $\{z_{\rm SSB} = 2.0, L = 1.0\}$ (bottom right). For each case we show the results for the two values $\beta = 0.5$ and $\beta = 1.0$.

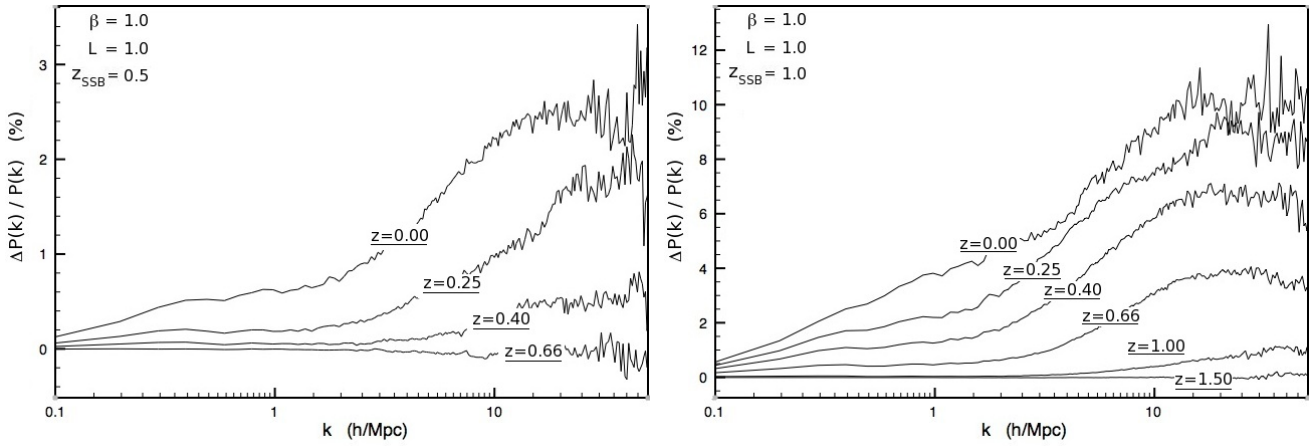

FIG. 13.— The fractional difference in the nonlinear power spectrum relative to ΛCDM for $\{z_{\rm SSB} = 0.5, L = 1.0, \beta = 1.0\}$ (left) and $\{z_{\rm SSB} = 1.0, L = 1.0, \beta = 1.0\}$ (right) for several different redshifts.

REFERENCES

Accetta, F. S., Krauss, L. M., & Romanelli, P. 1990, Physics Letters B, 248, 146

Adelberger, E. G. 2002, in CPT and Lorentz Symmetry, ed. V. A. Kostelecký, 9–15

Arkani-Hamed, N., Georgi, H., & Schwartz, M. D. 2003, Annals of Physics, 305, 96

Baldi, M. 2009, Nuclear Physics B Proceedings Supplements, 194, 178

Baldi, M., Pettorino, V., Robbers, G., & Springel, V. 2010, MNRAS, 403, 1684

Bertotti, B., Iess, L., & Tortora, P. 2003, Nature, 425, 374

Bertschinger, E. 2001, ApJS, 137, 1

Binetruy, P. 2006, Oxford, UK: Oxford Univ. Pr., 520p

Brax, P., Burrage, C., & Davis, A.-C. 2011a, ArXiv e-prints 1106.1573

Brax, P., Davis, A.-C., Li, B., Schmauch, B., & Shaw, D. 2011b, To appear in ArXiv e-prints

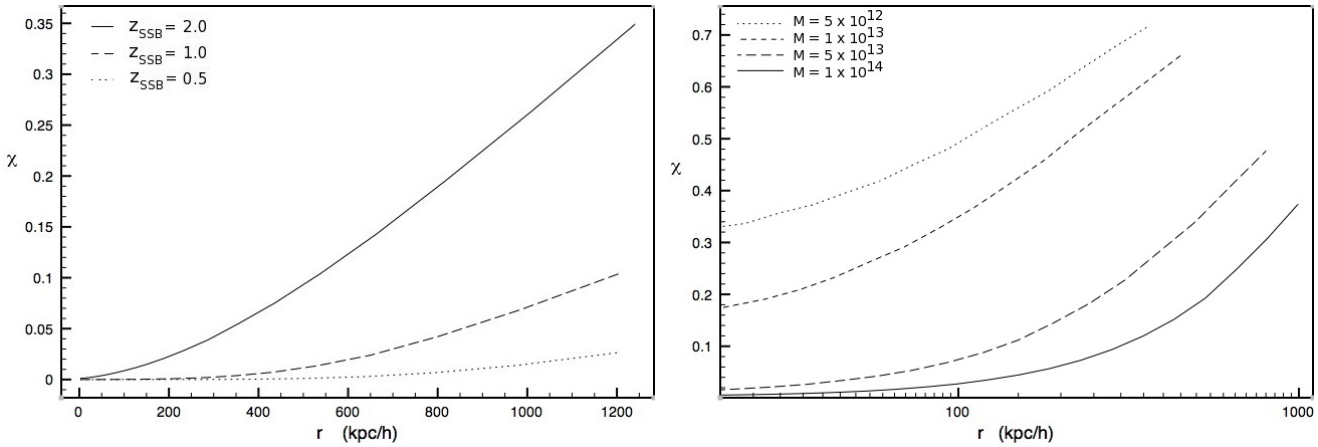

FIG. 14.— Left: the halo profile of χ in the most massive halo of the simulation for three different symmetry breaking redshifts. Right: the halo profile of χ for four halos of mass (from top to bottom) $M = \{5 \cdot 10^{12}, 10^{13}, 5 \cdot 10^{13}, 10^{14}\} M_{\rm sun}/h$ in the same simulation where $z_{\rm SSB} = 2.0$. In both cases we have fixed $\beta = L = 1$.

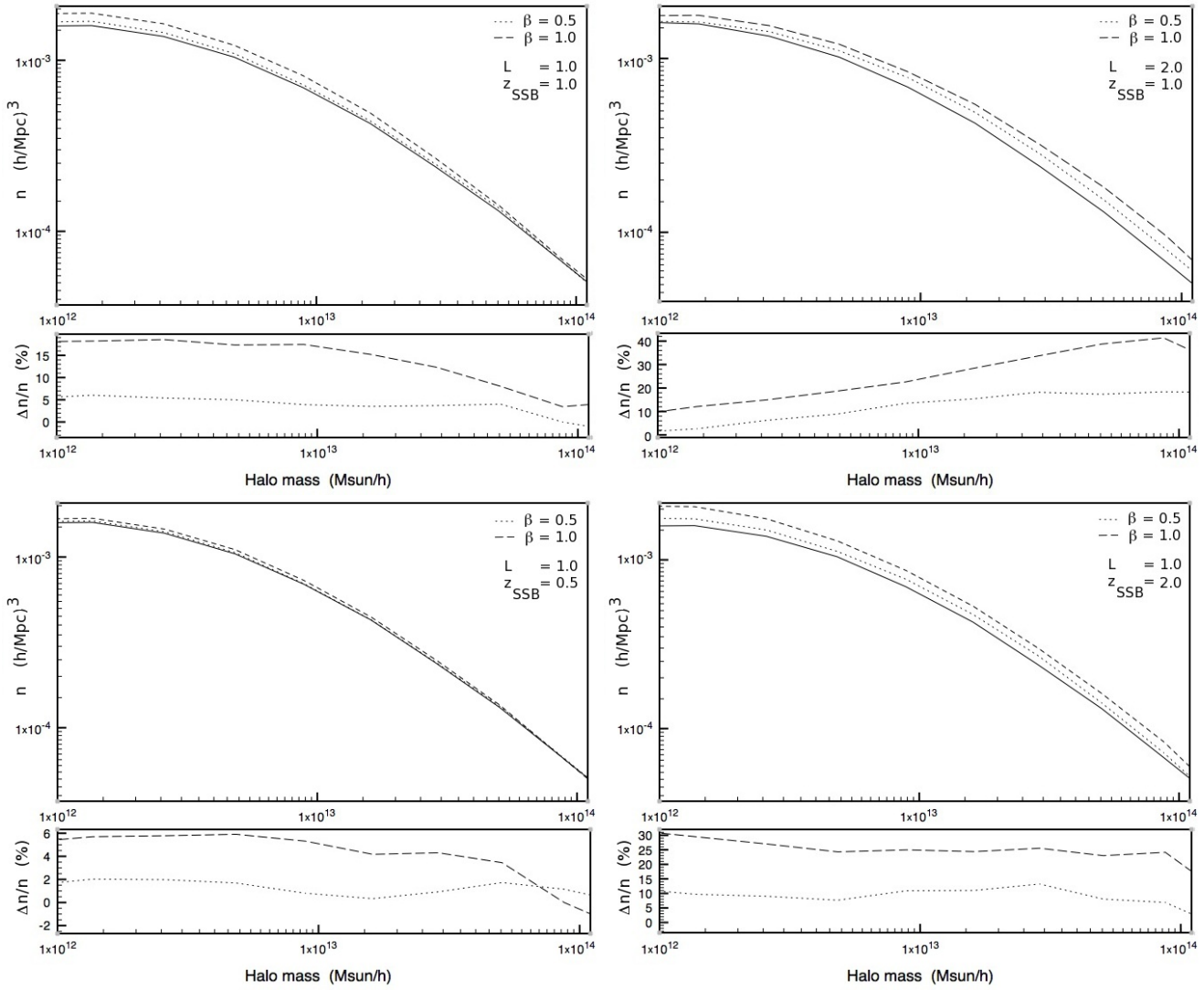

FIG. 15.— The halo mass function for $\{z_{\rm SSB} = 1.0, L = 1.0\}$ (top left), $\{z_{\rm SSB} = 1.0, L = 2.0\}$ (top right), $\{z_{\rm SSB} = 0.5, L = 1.0\}$ (bottom left) and $\{z_{\rm SSB} = 2.0, L = 1.0\}$ (bottom right). The solid black line shows the prediction of ΛCDM ($\beta = 0$) and the dotted and dashes lines are for the two values $\beta = 0.5$ and $\beta = 1.0$ respectively. We also show the fractional difference from ΛCDM. Note that we have smoothed the mass function over neighboring bins to remove noise arising from the binning as to show the trends more clearly.

Brax, P., van de Bruck, C., Davis, A.-C., Khoury, J., & Weltman, A. 2004, Phys. Rev. D, 70, 123518
Brax, P., van de Bruck, C., Davis, A.-C., Li, B., & Shaw, D. J. 2011c, Phys. Rev. D, 83, 104026
Brax, P., van de Bruck, C., Davis, A.-C., Mota, D. F., & Shaw, D. J. 2007a, Phys.Rev., D76, 124034
—. 2007b, Phys.Rev., D76, 085010
Brax, P., van de Bruck, C., Davis, A.-C., & Shaw, D. 2010a, JCAP, 4, 32
Brax, P., van de Bruck, C., Davis, A.-C., & Shaw, D. J. 2008, Phys. Rev. D, 78, 104021
Brax, P., van de Bruck, C., Mota, D. F., Nunes, N. J., & Winther, H. A. 2010b, Phys. Rev. D, 82, 083503
Clifton, T., Mota, D. F., & Barrow, J. D. 2005, Mon.Not.Roy.Astron.Soc., 358, 601
Colombi, S., Jaffe, A., Novikov, D., & Pichon, C. 2009, MNRAS, 393, 511
Davis, A.-C., Lim, E. A., Sakstein, J., & Shaw, D. 2011, ArXiv e-prints
de Rham, C. 2010, Physics Letters B, 688, 137
de Rham, C., Dvali, G., Hofmann, S., Khoury, J., Pujolas, O., Redi, M., & Tolley, A. J. 2008, PHYS.REV.LETT., 100, 251603
Decca, R. S., López, D., Fischbach, E., Klimchitskaya, G. L., Krause, D. E., & Mostepanenko, V. M. 2007, Phys. Rev. D, 75, 077101
Deffayet, C., Dvali, G., Gabadadze, G., & Vainshtein, A. 2002, Phys. Rev. D, 65, 044026
Dvali, G., Gabadadze, G., & Porrati, M. 2000, PHYS.LETT.B, 485, 208
Felder, G., Kofman, L., & Linde, A. 2001, PHYS.REV.D, 64, 123517
Gabadadze, G. 2009, Physics Letters B, 681, 89
Gannouji, R., Moraes, B., Mota, D. F., Polarski, D., Tsujikawa, S., & Winther, H. A. 2010, Phys. Rev. D, 82, 124006
Gies, H., Mota, D. F., & Shaw, D. J. 2008, Phys.Rev., D77, 025016
Gill, S. P. D., Knebe, A., & Gibson, B. K. 2004, MNRAS, 351, 399
Hinterbichler, K., & Khoury, J. 2010, Physical Review Letters, 104, 231301
Hinterbichler, K., Khoury, J., Levy, A., & Matas, A. 2011, ArXiv e-prints
Hinterbichler, K., Trodden, M., & Wesley, D. 2010, Phys. Rev. D, 82, 124018
Hoskins, J. K., Newman, R. D., Spero, R., & Schultz, J. 1985, Phys. Rev. D, 32, 3084
Hwang, J.-C., & Noh, H. 2002, Phys. Rev. D, 65, 023512
Khoury, J. 2010, ArXiv e-prints
Khoury, J., & Weltman, A. 2004, Phys. Rev. D, 69, 044026
Knebe, A., Green, A., & Binney, J. 2001, MNRAS, 325, 845
Li, B., & Barrow, J. D. 2011a, Phys. Rev. D, 83, 024007
—. 2011b, MNRAS, 413, 262
Li, B., Mota, D. F., & Barrow, J. D. 2011a, ApJ, 728, 109
—. 2011b, ApJ, 728, 108
Li, B., & Zhao, H. 2010, Phys. Rev. D, 81, 104047
Linde, A. 2008, in Lecture Notes in Physics, Berlin Springer Verlag, Vol. 738, Inflationary Cosmology, ed. M. Lemoine, J. Martin, & P. Peter, 1–+
Mota, D. F., & Barrow, J. D. 2004a, Mon.Not.Roy.Astron.Soc., 349, 291
—. 2004b, Phys.Lett., B581, 141
Mota, D. F., Sandstad, M., & Zlosnik, T. 2010, JHEP, 1012, 051
Mota, D. F., & Shaw, D. J. 2006, Phys.Rev.Lett., 97, 151102
Mota, D. F., & Shaw, D. J. 2007, Phys. Rev. D, 75, 063501
Mota, D. F., & Winther, H. A. 2011, ApJ, 733, 7
Nagata, R., Chiba, T., & Sugiyama, N. 2004, Phys. Rev. D, 69, 083512
Nicolis, A., Rattazzi, R., & Trincherini, E. 2008, The galileon as a local modification of gravity
Olive, K. A., & Pospelov, M. 2008, Phys. Rev. D, 77, 043524
Prunet, S., Pichon, C., Aubert, D., Pogosyan, D., Teyssier, R., & Gottloeber, S. 2008, ApJS, 178, 179
Tsujikawa, S., Gannouji, R., Moraes, B., & Polarski, D. 2009, Phys. Rev. D, 80, 084044
Vainshtein, A. I. 1972, Physics Letters B, 39, 393
Zhao, G.-B., Li, B., & Koyama, K. 2011a, Phys. Rev. D, 83, 044007
—. 2011b, ArXiv e-prints
Zhao, H., Macciò, A. V., Li, B., Hoekstra, H., & Feix, M. 2010, ApJ, 712, L179